

An Energy Storage System Based on Iron Fuel

Parinaz Farhadi



Department of Mechanical Engineering
McGill University
Montréal, Québec, Canada

August 15, 2023

A thesis presented for the degree of Masters of Mechanical Engineering

©2023 Parinaz Farhadi

Abstract

Fossil fuels are the major sources of energy today since they are cost-effective, easy to transport, and energy dense. On the other hand, fossil fuels have limited reserves, and burning them produces carbon dioxide, contributing to climate change. Thus, shifting towards a new sustainable and environmentally friendly source of energy, such as solar, wind, and hydropower, is essential. An energy carrier should be deployed to store the energy of these intermittent renewable resources and transport it across the globe. In this manner, using metal powders as fuels has been investigated over the last decades, i.e., metal powders are oxidized and produce energy over peak demand, and subsequently, the oxidized powders are captured and reduced during peak production.

This thesis focuses on building a novel apparatus to demonstrate the gradual oxidation of iron powders in a packed bed without melting. The process starts with heating iron powders to 500°C via an electric heater. Then, the air is fed into the preheated bed, and the oxidation zone slowly propagates from the air inlet to the opposite end of the bed. The burner is built at the lab scale, i.e., about 50 g of iron powder is used in each experiment. Magnetite is considered the main product of combustion, and the combustion efficiency is determined above 80%. Moreover, tube diameter, air flow rate, the temperature of the heater, and the composition of powders are found to be the parameters controlling this reaction.

Abrégé

Les combustibles fossiles sont aujourd'hui les principales sources d'énergie car ils sont économiques, faciles à transporter et ont une forte densité énergétique. D'autre part, les combustibles fossiles ont des réserves limitées et leur combustion est la principale source d'émissions de dioxyde de carbone, contribuant au changement climatique. Ainsi, la transition vers une nouvelle source d'énergie durable et respectueuse de l'environnement, comme le solaire, l'éolien et l'hydroélectricité, est essentielle. De plus, un vecteur énergétique devrait être déployé pour stocker l'énergie de ces ressources renouvelables intermittentes et la transporter dans le monde entier. Ainsi, l'utilisation de poudres métalliques comme combustibles a été étudiée au cours des dernières décennies. Lorsqu'oxydées, ces poudres métalliques produisent de l'énergie qui peut satisfaire les pics de demande. Ensuite, les poudres oxydées sont réduites lors des pics de production.

Cette thèse porte sur la construction d'un nouvel appareil pour démontrer l'oxydation progressive de poudre de fer en lit tassé, sans fusion du carburant. Le processus commence en chauffant les poudres de fer à 500°C grâce à un radiateur électrique. Ensuite, de l'air est introduit dans le lit préchauffé et les poudres de fer sont graduellement oxydées dans une zone se propageant de l'entrée d'air jusqu'à la sortie du réacteur. Le brûleur est construit à échelle de laboratoire, c'est-à-dire qu'environ 50 g de poudre de fer sont utilisés dans chaque expérience. La magnétite est considérée comme le principal produit de combustion et le rendement de combustion est de plus de 90 %. De plus, le diamètre du tube, le débit d'air,

la température du préchauffeur et la composition des poudres ont été identifiés comme étant les paramètres contrôlant cette réaction.

Acknowledgement

First and foremost, I am extremely grateful to my supervisor, Prof. Jeffrey M. Bergthorson, for his precious advice, continuous support, and patience throughout the course of my studies. His immense knowledge helped me to overcome the challenges faced in this research, and his positivity and kindness encouraged me to work harder and do my best.

I would also like to thank Dr. Jan Palecka and Julien Otis-Laperriere for all their help with this research, and I want to extend this thanks to my friends, lab mates, and colleagues at AFL for their guidance and the cherished time spent together.

Lastly, I would like to express my gratitude to my parents, Fariba and Farzin, and my elder sister, Parim. Everything I have achieved in my entire life would not be possible without their tremendous support and encouragement.

Contents

1	Introduction	1
1.1	Metal Fuels	1
1.2	Metal Combustion	5
1.3	Metal-based Burners	7
1.3.1	Chemical Looping Reactors	8
1.3.2	Turbulent Burner	11
1.4	Filtration Combustion	12
1.5	Smouldering Combustion	14
1.6	Fundamentals of Iron Oxidation	15
1.7	Objectives	17
2	Apparatus	20
2.1	Preheating	20
2.1.1	Methane Air Flame	20
2.1.2	Electric Heater	22
2.2	Sealing	24
2.3	Mass Flow Controller	28
2.4	Powders	29
2.5	Pressure Drop	30

3 Experiments	33
3.1 First Campaign: Preheating Bed via Methane Air Flame	33
3.1.1 Methodology	33
3.1.2 Results and Discussion	34
3.2 Second Campaign: Preheating Air via Electric Heater	36
3.2.1 Methodology	36
3.2.2 Results and Discussion	38
3.3 Third Campaign: Preheating Bed via Electric Heaters	40
3.3.1 Methodology	41
3.3.2 Results and Discussion	42
4 Conclusion	67

List of Figures

1	World crude oil production, plotted by King Hubbert. According to his prediction, oil production will be zero by the year 2200. Reprinted from [2]	2
2	Yearly surface temperature compared to the 20 th century average from 1880-2022, plotted by NOAA[3]	2
3	The fuel should have high specific energy (only elements in periods 1-4 are considered) and react with air (groups 15-18 are faded). It should not be rare (colored gold), toxic, or produce toxic compounds in the reaction with oxygen (colored yellow). Furthermore, hydrogen is eliminated due to its low energy density and storage challenges. Reprinted from [19]	3
4	Energy density and specific energy of various metals compare to hydrocarbons, liquid hydrogen, Li batteries, and PCMs. Adopted from [19]	4
5	Metal Fuel Cycle. Reprinted from [20]	4
6	The amount of metal fuels reserves and quantities required to power world yearly	5
7	Combustion modes of particles burning in the small Biot number regime. Reprinted from [28]	7
8	Scheme of CLC process.	9
9	Scheme of a slice of the novel CLC reactor suggested by Abanades et al. [40]. Reprinted from [41]	10

10	An energy storage system based on the novel CLC reactor suggested by Abanades et al. [40] with high-power discharging lasting short periods of time, followed by long charging to reduce the oxidised metal. Reprinted from [41]	10
11	Some metal-fuels flames stabilized on a costum-built bunsen burner compared to a mathane-air Bunsen flame. Reprinted from [28]	11
12	Concept of the turbulent burner and its possible applications at a range of power-generation scales. Reprinted from [28]	11
13	Filtration combustion: a)Natural filtration combustion b)Co-flow filtration combustion c)Counter-flow filtration combustion	13
14	Flaming combustion vs smouldering combustion in organic soil. Reprinted from [53]	14
15	Iron phase diagram. Reprinted from [58]	16
16	A cross-section view of an iron oxide sample. Reprinted from [26]	16
17	Scheme of the packed bed burner during a)Discharging (oxidation) b)Charging (reduction)	18
18	The reactor used in the first campaign	21
19	A simple sketch of the apparatus used in the first campaign	21
20	The apparatus used in the second campaign	22
21	A simple sketch of the apparatus used in the second campaign	23

22	The apparatus used in the third campaign	23
23	A simple sketch of the apparatus used in the third campaign	24
24	The apparatus used in the experiments	25
25	An SEM image taken from iron powders	30
26	Pressure drop in a packed bed consists of spherical particles with $d = 300 \mu\text{m}$ while the airflow rate is 3.5 cm/s	32
27	Diagram of the first campaign apparatus	33
28	The combustion front, first campaign	34
29	An oxidized iron bed produced in the first campaign	35
30	Colourful iron hydroxides ($\text{Fe}(\text{OH})_2$ and $\text{Fe}(\text{OH})_3$) produced during the preheating process.	36
31	Diagram of the second campaign apparatus	37
32	Temperature of the bottom (T1) and top (T2) of the iron bed in one of the tests in the second campaign	38
33	Melting within the bed in one of the tests of the second campaign	39
34	Placing ceramic wool as thermal insulation around the quartz tube to reduce the heat loss to the environment	40
35	Diagram of the final apparatus	41
36	Cylindrical rod with internal heat generation [75]	43

-
- 37 IR images showing the combustion zone in two different tests with various powder composition: a) No ceramic powders used. b) 10% of the volume of the bed consists of ceramic. Temperature bar is in Kelvin. 46
- 38 The maximum surface temperature which does not lead to melting inside the bed over the tube's diameter for a pure iron bed and when 10% of the volume of the bed consists of ceramic powders. 47
- 39 a)The gas channels resulted from melting inside the bed is observed in the oxidised bed when no ceramic powders mixed with iron powders. b)No melting is observed when 10% of the volume of the bed consists of ceramic powders, airflow rate = 10 cc/s and combustion chamber's diameter = 1.9 cm. 48
- 40 Combustion front propagation during one test. The bed consists of iron powders (no ceramic is used) and airflow rate is 10 cc/s. Shots are taken in equal time steps. 49
- 41 Combustion front propagation during two different tests: 40% of the volume of the bed consists of ceramic powders, and airflow rate is a)10 cc/s and b)15 cc/s. Temperature bar is in Centigrade, and shots are taken in equal time steps. 50
- 42 IR images of different tests over 30 minutes: airflow rate is 10 cc/s, and the CVR is different between 0% and 60%. Temperature bar is in Centigrade, and shots are taken in equal time steps 52

43	Oxidized bed produced in different tests with various powder compositions. Airflow rate is 10 cc/s, and the CVR is different between 0% and 60%	53
44	Combustion efficiency of different powder compositions, calculated according to the mass of the oxidized bed vs. results of the XRD analysis.	57
45	Time of the tests of various powder compositions.	59
46	Propagation speed of the reaction wave of different powder composition . . .	60
47	Conversion rate of iron to the iron oxides of different powder compositions .	61
48	Pressure over the bed during test for various powder composition (CVR=0 to 60%)	64

List of Tables

1	Parameters for the parabolic growth of FeO and Fe ₃ O ₄ [26].	17
2	Results of screen analysis of iron powders provided by the supplier [68] . . .	29
3	Range of the airflow rate tested in the first campaign	34
4	Results of the tests with various powder compositions, campaign 3	51
5	Results of the XRD analysis conducted on the oxidized powders of various tests. Airflow rate is 10 cc/s, and the CVR is different between 0% and 60%.	54
6	Determining the mass of the initial bed for 100g oxidized powders according to the XRD results.	56

7 Properties of air and iron bed. Note that the density of a bed consisting of iron powders is considerably lower than the density of iron due to the porosity of the bed and powders. 59

1 Introduction

1.1 Metal Fuels

Mankind has tried to find a sustainable source of energy since the earliest time, as energy consumption and prosperity are highly correlated. In the 1770s, James Watt used coal to produce power in a steam engine, and in the 1880s, coal was first consumed to generate electricity. Now, fossil fuels (coal, natural gas, and oil) are the main sources of energy as they are cost-effective, easy to transport, and energy dense. However, a shift towards new energy resources is essential since fossil fuels have finite reserves (Fig. 1). Moreover, the combustion of fossil fuels produces carbon dioxide, contributing to climate change due to its greenhouse effect, i.e., the global average surface temperature significantly increased over the last century (Fig. 2), and an immediate and all-inclusive solution is required to limit global warming to 1.5°C or 2°C [1].

Over the last decades, different methods such as carbon capture [4, 5] have been proposed to reduce the CO₂ emissions of fossil fuels burning. Additionally, scientists all over the world investigated sustainable and environmentally friendly sources of energy such as solar [6, 7], wind [8, 9], and hydro power [10, 11]. There are two major problems in using these resources: they are intermittent, and some areas do not have access to sufficient sources of renewable energy, so the energy generated in other regions should be transported to these areas.

To address these issues, several solutions have been investigated, such as use of hydrogen [12,

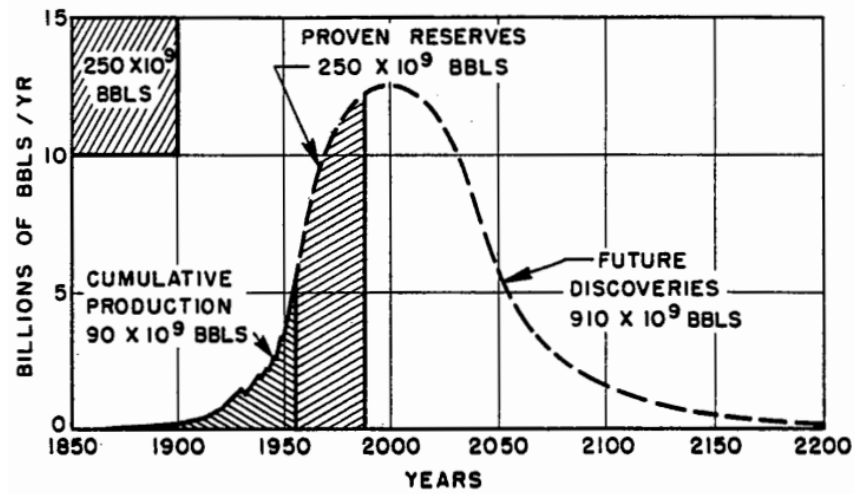


Figure 1: World crude oil production, plotted by King Hubbert. According to his prediction, oil production will be zero by the year 2200. Reprinted from [2]

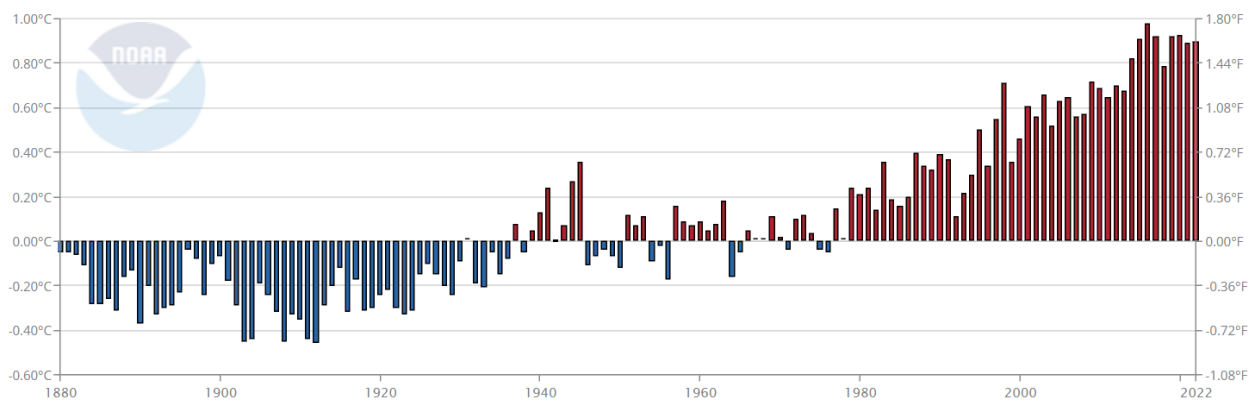


Figure 2: Yearly surface temperature compared to the 20th century average from 1880-2022, plotted by NOAA[3]

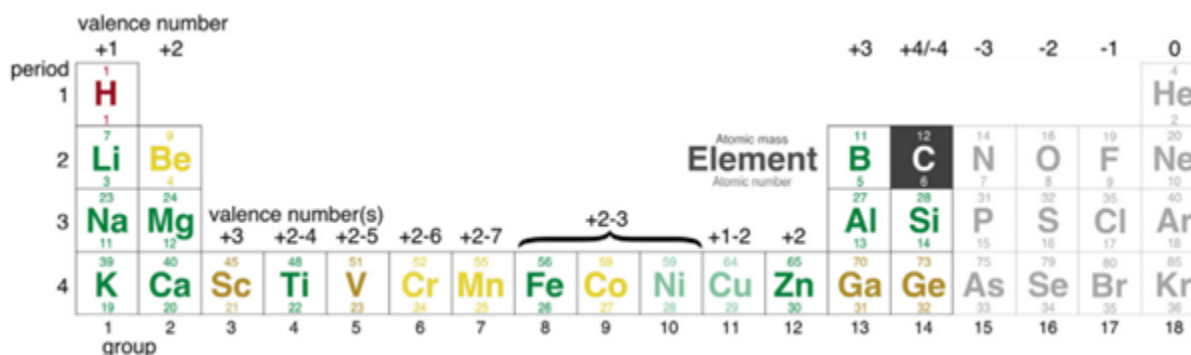


Figure 3: The fuel should have high specific energy (only elements in periods 1-4 are considered) and react with air (groups 15-18 are faded). It should not be rare (colored gold), toxic, or produce toxic compounds in the reaction with oxygen (colored yellow). Furthermore, hydrogen is eliminated due to its low energy density and storage challenges. Reprinted from [19]

[13] or lithium-ion batteries [14, 15]. Moreover, storing heat by Phase Change Materials (PCMs) [16, 17, 18] is encouraged over the last decades.

J.M. Bergthorson proposed the use of metal fuels as a clean and compact source of energy [19]. He identified specific features that an ideal energy carrier should have, such as high specific energy, reactivity with air, low price, and non-toxicity. Based on these criteria, he narrowed down the elements of the periodic table that could potentially be used as fuels to those colored green in Figure 3, and all these fuel options are metal.

Another important factor for an ideal fuel is having high energy density, enabling easy transportation. As Figure 4 illustrates, the energy densities of metals, such as iron and aluminum, are considerably higher than hydrocarbon fuels, liquid hydrogen, and other zero-carbon options, including PCMs and Li-ion batteries.

Metals can burn in air or react with water to produce heat, and the main product of these

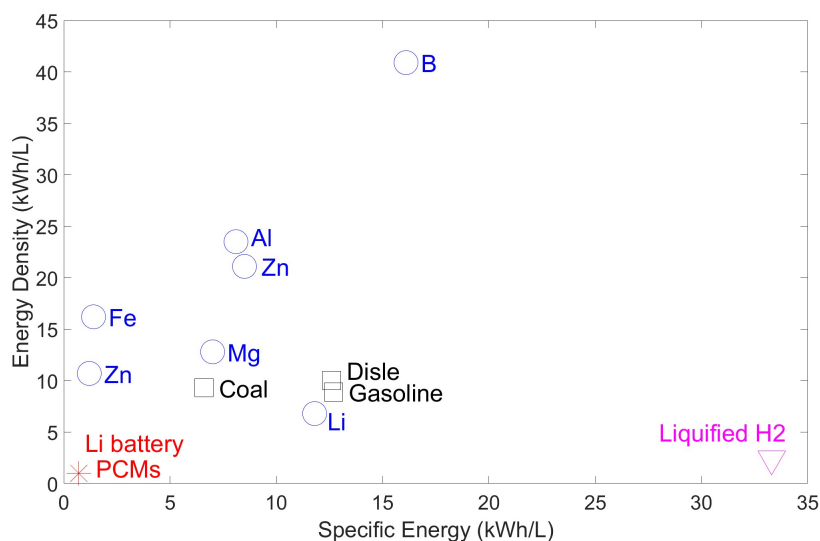


Figure 4: Energy density and specific energy of various metals compare to hydrocarbons, liquid hydrogen, Li batteries, and PCMs. Adopted from [19]

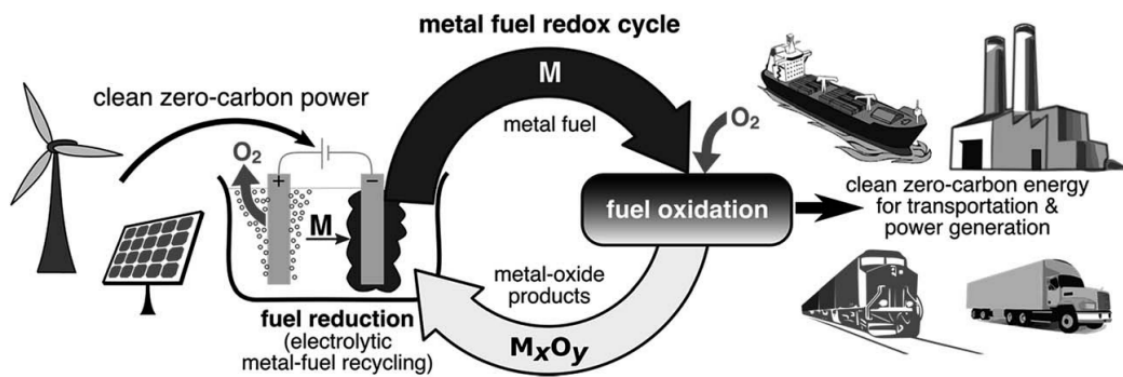


Figure 5: Metal Fuel Cycle. Reprinted from [20]

reactions is solid metal oxides that can be reduced. This reduction allows the metals to be recycled and used repeatedly (Fig. 5).

Figure 6 demonstrates the amount of some of the metals reserves compared to the amount of fuel required to power the world over a year. According to this figure, there are enough

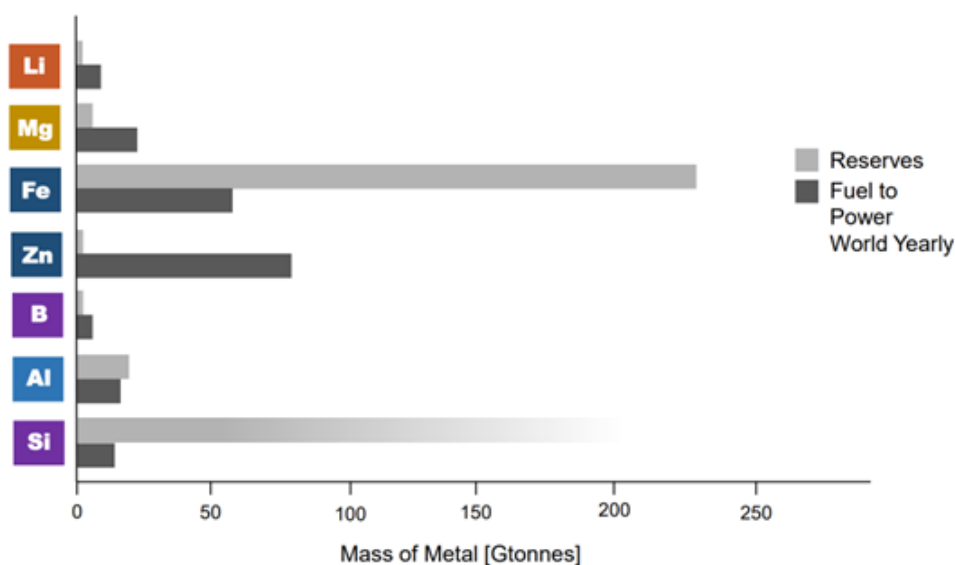


Figure 6: The amount of metal fuels reserves and quantities required to power world yearly iron, aluminum, and silicon reserves to provide energy for the whole world for a year.

In conclusion, the ability to take part in the oxidation/reduction reactions along with the low cost, abundance (Fig. 6), and high energy density (Fig. 4) motivates the use of metals such as iron and aluminum as fuels.

1.2 Metal Combustion

For developing energy systems based on metal fuels, a fundamental understanding of the combustion process is essential.

The combustion of solid particles is controlled by two processes: the rate of the reaction and the diffusion of the oxidizer to the particle surface. These processes determine whether the system is in a kinetically limited regime, where the reaction rate is slower than the

transportation of oxidizer, or a diffusion-limited regime, where the reaction rate is faster than the oxidizer can be transported to the particle surface. This also affects the temperature of the particle, which is around the bulk gas temperature in a kinetically limited regime or roughly equal to the stoichiometric flame temperature in a diffusion-limited regime [21].

Initially, a particle starts reacting in the kinetically limited regime and releases heat. The temperature of the particle increases if the generated heat is higher than the heat loss, causing an exponential rise in the reaction rate (Arrhenius equation), and the diffusion of the oxidizer becomes the rate-limiting step. Generally, ignition is considered this transition from kinetic to diffusion-limited combustion [21]. Over the last decades, the ignition of metal particles has been investigated experimentally and qualitatively in various research [22, 23, 24, 25], and Mi et al. [26] recently suggested a successful model for analyzing the ignition of fine iron particles.

After the reaction onset, small metal particles with a low Biot number can burn in different modes depending on the flame temperature and boiling point. According to Glassman [27], if the metal's flame temperature and oxide-volatilization point exceed its boiling point, the metal will vaporize and react in the vapor phase (Fig. 7A). However, if the flame temperature is less than the boiling point, the metal will burn heterogeneously on the particle surface. This heterogeneous combustion can occur in two modes (B and C), as illustrated in Figure 7. In mode B, the gaseous metal oxides and sub-oxides are produced on the metal surface. These gaseous products condensate again and form nano-oxides away from the particle surface. On

the other hand, in mode C, the oxides are formed directly on the metal surface and create a porous solid metal oxide shell, leading to a metal oxide particle larger than the initial metal particle, i.e., the Pilling-Bedworth ratio is greater than 1.

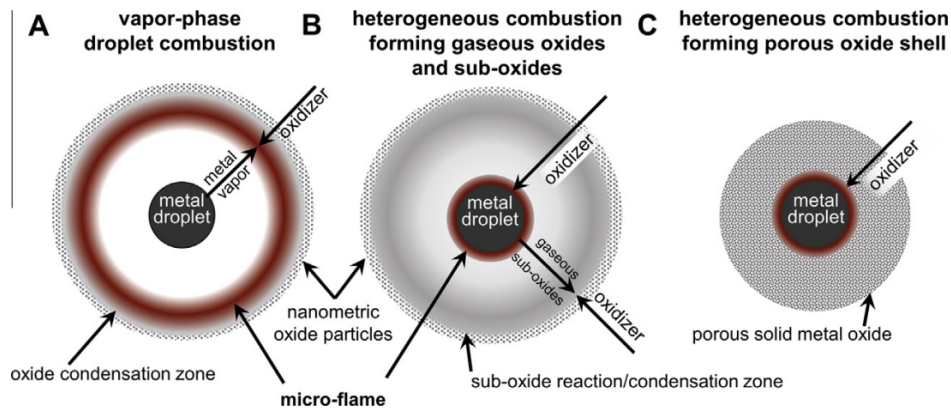


Figure 7: Combustion modes of particles burning in the small Biot number regime. Reprinted from [28]

1.3 Metal-based Burners

The use of metals in energy generation systems, such as chemical looping reactors and turbulent burners, has been investigated in recent decades. While these technologies have the potential to provide clean energy, there are still in the research stage and several technological challenges are needed to be addressed before they can be applied in a practical energy generation system.

1.3.1 Chemical Looping Reactors

The concept of chemical looping was first proposed in a patent in 1954 [29]. It involves using solid oxygen carriers in redox cycles to separate carbon dioxide from other combustion products. The process typically consists of two reactors: the fuel reactor and the air reactor. In the air reactor, the oxygen carrier is oxidized, and in the fuel reactor, it is reduced by releasing oxygen to a reducing gas. Metal oxides, such as copper oxide (CuO), manganese oxide (Mn₂O₃), and iron oxide (Fe₂O₃), are often used as oxygen carriers in this process [30]. The chemical looping conversions can be utilized for various purposes, such as the production of syngas through chemical looping reforming (CLR) [31, 32] and gasification (CLG) [33, 34], or hydrogen generation (CLHG) [35, 36].

Another technology based on this conversion is Chemical Looping Combustion (CLC) [37, 38] in which the metal oxides transfer oxygen from air to fuel, such as coal or natural gas, to produce energy. The exit gases from the fuel reactor are just CO₂ and water vapor, which are not diluted by atmospheric N₂ as the use of oxygen carriers prevents direct contact between fuel and air. Thus, the main advantage of CLC is that it can produce almost pure CO₂ after condensing water vapor, making it an effective method for carbon capture. Figure 8 illustrates the principle of a chemical looping combustion system.

Noorman et al. [39] proposed using packed bed reactors in CLCs, wherein the reactive particles remain stationary while the oxidizing/reducing gases flow alternately over the bed. Compared to the fluidized bed, the advantage of this system is that no extra energy input is

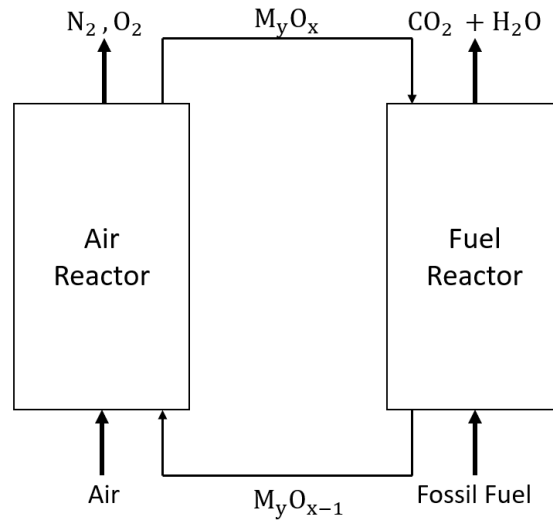


Figure 8: Scheme of CLC process.

required to transport the powders. Moreover, the fluidized bed setup requires the attachment of a cyclone to separate the powders from the gas stream, making the packed bed system more compact.

Abanades et al. [40] recently proposed a novel packed CLC system which contains several perforated air conduits within a packed bed of metal (Fig. 9). The pressurized air passes through these conduits, and oxygen transports to the fuel via the orifices following Fick's law while the net flow of nitrogen is zero, i.e., inside and outside of the conduits are at the same pressures, and metals inside the bed consume oxygen, causing a diffusive flow of oxygen due to the gradient of the concentration.

Subsequently, a reducing gas, such as biomass or hydrogen, passes through the conduits and reduces the oxidized metals. Thus, this technology can work as an energy storage system

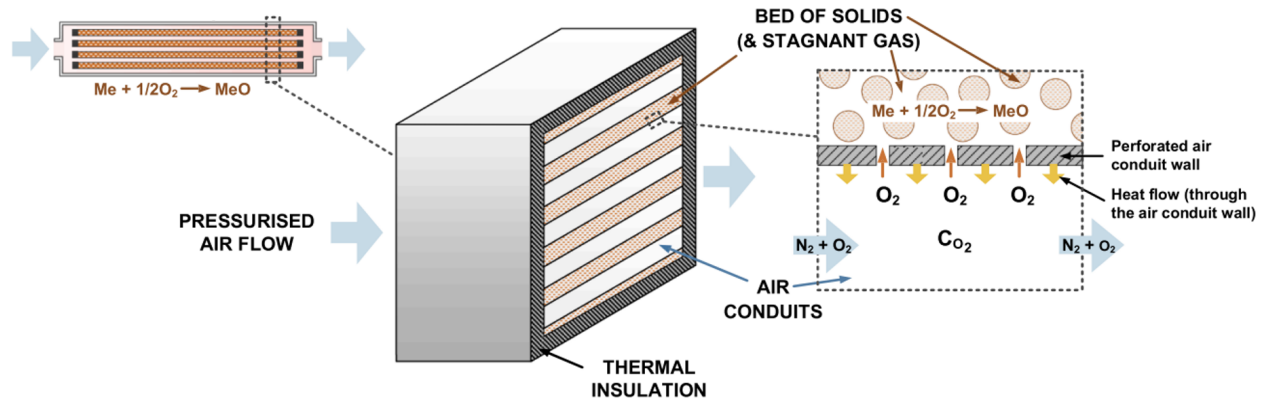


Figure 9: Scheme of a slice of the novel CLC reactor suggested by Abanades et al. [40]. Reprinted from [41]

to be cyclically charged (reduced) and discharged (oxidized), as Figure 10 illustrates. Diego et al. demonstrated the slow oxidation of graphite in a lab-scale size of this burner [41]. Furthermore, he did a techno-economic analysis to show this burner can be used as an energy storage system in off-grid power plants[42].

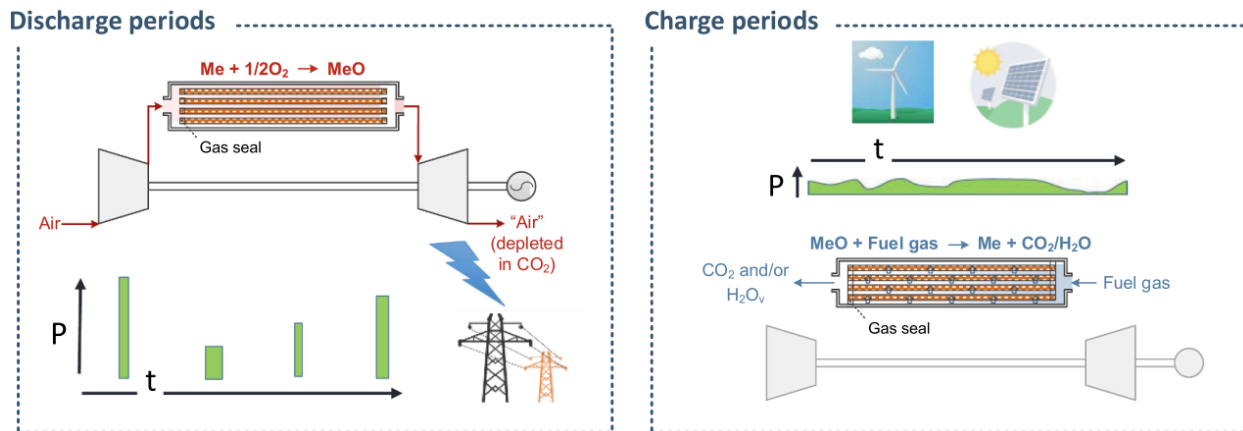


Figure 10: An energy storage system based on the novel CLC reactor suggested by Abanades et al. [40] with high-power discharging lasting short periods of time, followed by long charging to reduce the oxidised metal. Reprinted from [41]

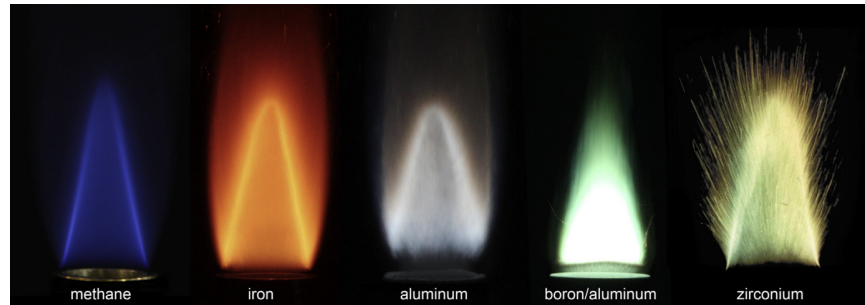


Figure 11: Some metal-fuels flames stabilized on a custom-built bunsen burner compared to a methane-air Bunsen flame. Reprinted from [28]

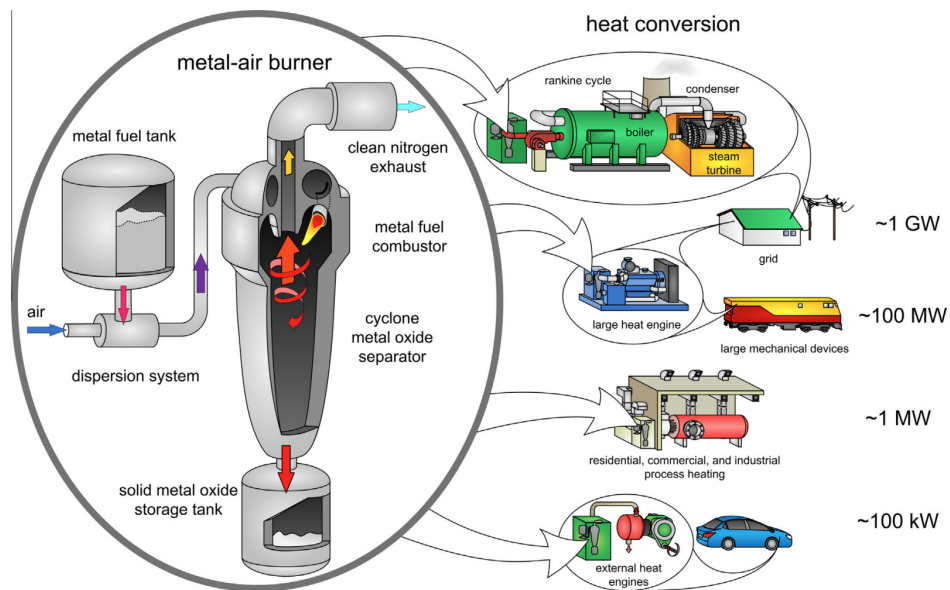


Figure 12: Concept of the turbulent burner and its possible applications at a range of power-generation scales. Reprinted from [28]

1.3.2 Turbulent Burner

As shown in Figure 11, metal particles can be burned in direct contact with air or other oxidizers to produce a stabilized flame.

Bergthorson et al. [28] proposed the use of a turbulent burner to generate power from metal

powders as they can react with air at a desirable and controllable combustion rate, similar to hydrocarbon fuels. The turbulent burner consists of a metal fuel tank, a powder-dispersion system, a cyclonic solid-combustion-product separator, and a storage tank for the metal oxide (Fig. 12). The energy is generated in the burner through the reaction between the dispersed metal powders and air, and the cyclone phase-separation technology is used to capture the produced metal oxides for recycling.

1.4 Filtration Combustion

Filtration combustion (FC) is a process in which a flow of gas infiltrates into a packed bed of powders. It is a type of self-propagating high-temperature synthesis (SHS) [43] and can be distinguished into natural FC and forced FC. In natural FC, the gas is supplied from the surrounding through natural infiltration, i.e., the consumption of gas in the reaction zone decreases the pressure inside the bed, causing the surrounding gas to infiltrate into the porous reagent (Fig. 13a), and in forced FC, a flow of gas is fed into a packed porous bed.

Depending on the direction of the gas flow and reaction propagation, two configurations are considered in filtration combustion: co-flow and counter-flow, i.e., the direction of the reaction zone propagation and the oxidizer flow are the same in the co-flow (Fig. 13b) while their directions are opposite in the counter-flow (Fig. 13c).

The theory of filtration combustion in metals was first studied by Aldushin et al. in 1976 [44]. Bayliss et al. [45] recently suggested a mathematical model for natural counter-flow

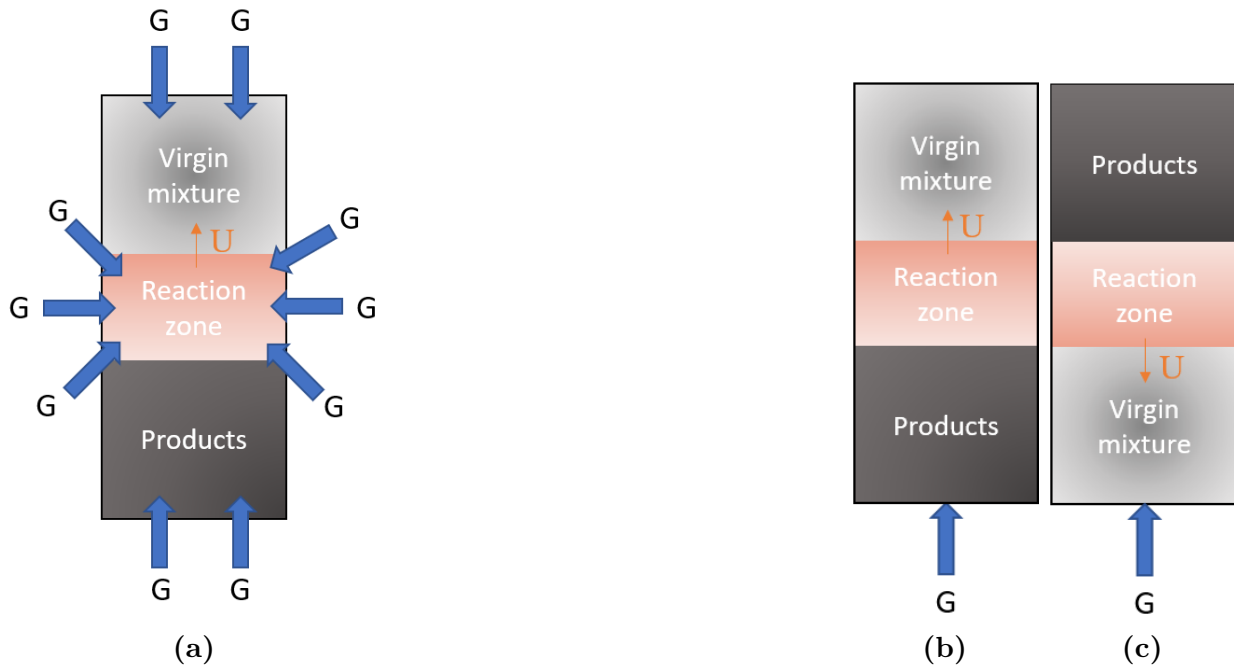


Figure 13: Filtration combustion: a) Natural filtration combustion b) Co-flow filtration combustion c) Counter-flow filtration combustion

filtration combustion, and Cordova et al. [46] did experimental studies on natural counter-flow filtration combustion of magnesium which can be used to produce energy in space. Moreover, filtration combustion of titanium powders was studied in various investigations [47, 48, 49]. In this thesis, forced filtration combustion of iron powders is experimentally investigated.

Note that filtration combustion can also refer to a process in which a mixture of gaseous reactants infiltrates into a porous reactor. This technology is known as a heat recirculating reactor which recycles the energy produced in the combustion by preheating the reactants with it [50, 51], and it is not investigated in this research.

1.5 Smouldering Combustion

Another form of combustion that can occur in porous fuels is smouldering, in which solid porous hydrocarbons such as coal, wood, and organic fibers are oxidized in a slow, low-temperature, and flame-less exothermic reaction.

In flaming combustion of hydrocarbons, the oxidizer reacts with fuel in the gas phase (similar to mode A), while in smouldering combustion, the oxidation takes place on the solid surface of the fuel (Fig. 14). Generally, smouldering operates under oxygen-limiting conditions, and increasing the air flux leads to a transition to flaming combustion [52].



Figure 14: Flaming combustion vs smouldering combustion in organic soil. Reprinted from [53]

Smouldering combustion has been mostly studied from a fire-safety perspective due to its residential and environmental hazards, i.e., smouldering combustion triggers a considerable amount of residential fires [54] and wildfires [55] since it is not detectable or extinguishable

via conventional methods.

There are critical differences between the combustion phenomena observed in this thesis and smouldering combustion, e.g., pyrolysis is an important step during smouldering, which does not happen in metal combustion. However, it is still a valuable analog as in these experiments, the iron powders burn at low temperatures due to the lack of oxidizer.

1.6 Fundamentals of Iron Oxidation

The mentioned combustion modes and ignition theory cannot be applied to this research as the temperature is kept relatively low; therefore, the kinetic rate does not considerably increase (Arrhenius equation), and the iron particles do not ignite. In this section, the theory of high-temperature oxidation of iron is briefly discussed.

Wüstite (FeO), magnetite (Fe_3O_4), and hematite (Fe_2O_3) are different types of iron oxides (Fig. 15). Wüstite is mostly referred to as FeO , but it is actually Fe_{1-x}O where x varies at any given temperature. Wüstite stability expands at higher temperatures, and it is not stable below $570\text{ }^\circ\text{C}$. Magnetite (black to gray oxide) and hematite (reddish brown oxide) are the most common forms of the iron oxide existing naturally.

Paidassi found the thicknesses of the Fe_2O_3 , Fe_3O_4 , and FeO layers at 700 to $1250\text{ }^\circ\text{C}$ are 1% , 4% , and 95% of the overall thickness of the oxide, respectively (Fig. 16) [56]. At 570 - $700\text{ }^\circ\text{C}$, various thickness ratios of the oxides layers were observed in different studies [57], and at below $570\text{ }^\circ\text{C}$, scale structure is completely different as Wüstite is not stable at this

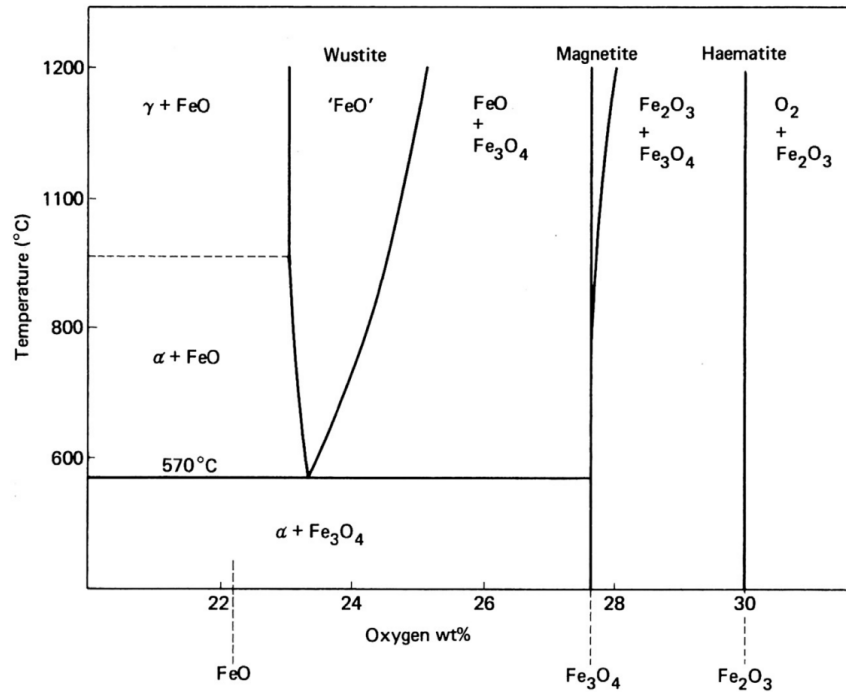


Figure 15: Iron phase diagram. Reprinted from [58]

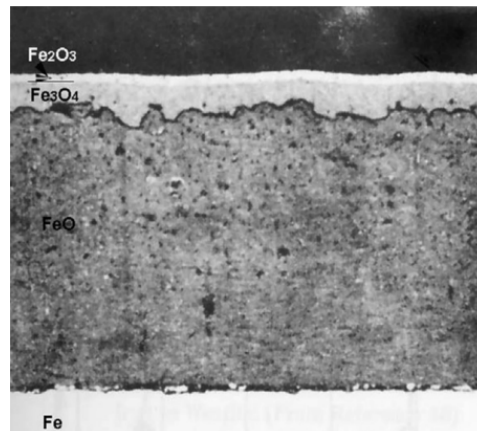


Figure 16: A cross-section view of an iron oxide sample. Reprinted from [26]

temperature range.

According to Wagner's theory, the growth of the oxide layers depends on the diffusivity of

ions and follows the parabolic law [59]. Wagner's theory was extended to the growth of a multilayered oxide film on iron, i.e., the growth of each oxide layer in iron oxides relates to the diffusion of Fe cations in the oxide layers [60, 61]:

$$\frac{dX_i}{dt} = \frac{k'_{x,i}}{X_i} \rightarrow X_i^2 = k_{x,i}t + X_{i,0}^2 \quad (1)$$

Where X_i is the thickness of the oxide layer, $k_{x,i}(= 2k'_{x,i})$ is the parabolic rate constant, $X_{0,i}$ is the initial scale thickness, and i is the index of each oxide layer. Moreover, $k'_{x,i}$ depends on the temperature by an Arrhenius function [62]:

$$k'_{x,i} = k_{0,i} \exp\left(\frac{-T_{a,i}}{T}\right) \quad (2)$$

Where $k_{0,i}$ is a constant and $T_{a,i}$ is the activation temperature for the growth of oxide layers.

The values of k_0 and T_a for FeO and Fe₃O₄ is reported in Table 1.

	$k_0(\text{m}^2\text{s}^{-1})$	T_a (K)
FeO	2.670×10^{-4}	20319
Fe ₃ O ₄	1.027×10^{-6}	21310

Table 1: Parameters for the parabolic growth of FeO and Fe₃O₄ [26].

1.7 Objectives

According to the previous sections, iron is a promising fuel for a zero-carbon future, and different systems, including CLC and turbulent burner, were suggested for generating power

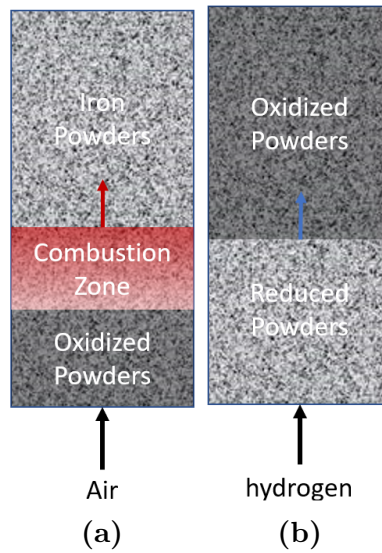


Figure 17: Scheme of the packed bed burner during a) Discharging (oxidation) b) Charging (reduction)

through iron combustion.

This research proposes a novel technology based on iron that can release heat at a controllable rate and relatively low temperature. In this burner, a small flow rate of air is fed into a packed porous bed of iron powders (forced filtration combustion), and oxidation starts. The temperature and the rate of the reaction are kept low by restricting the oxidizer flow (smouldering combustion).

Similar to the CLC system illustrated in Figure 10, once the iron powders are fully burned, hydrogen is fed into the bed to reduce the oxidized powders. Thus, this burner works between oxidation and reduction cycles and is successively discharged and charged (Fig. 17).

This system does not require the permeable conduits of the Abanades et al. [40] setup (Fig. 9), reducing the cost and complexity of the production. Moreover, using iron powders in the

turbulent burner leads to a combustion temperature over 2200 K [28], causing thermal NO_x emission, while in this burner, no pollutants are produced as the low operating temperature prevents NO_x formation.

The scope of this thesis is:

- Demonstrating low-temperature and slow filtration combustion of iron powders.
- Identifying the key parameters controlling this reaction.

In order to achieve the mentioned goals, an apparatus is designed and built, enabling the filtration combustion of iron powders. Then, various experiments were conducted to gain a better understanding of this reaction, i.e., the effect of powder composition and the airflow rate was investigated by measuring different parameters, including combustion temperature, time of the reaction, combustion efficiency, speed of the combustion wave, rate of iron consumption, and pressure drop over the bed.

2 Apparatus

This apparatus consists of a porous packed bed of iron powders which react with air to release heat in a controllable rate and relatively low temperature.

In this chapter, different aspects of this setup, such as its design and any potential limitations or challenges associated with it, are discussed.

2.1 Preheating

The reactants (iron powders and air) must be heated in order for the combustion reaction to start. This can be done by using various heating methods, such as heating iron powders via an induction heater, an electric heater, or a flame (such as a methane/air flame). Additionally, it is also possible to heat the input air using an electric heater, as this has been tested in a few experiments. Once the reaction initiates, it becomes self-sustaining, meaning that the produced energy is enough to keep it going.

2.1.1 Methane Air Flame

Using a methane/air flame for preheating the iron bed is a possible method for initiating the combustion reaction. Fig. 18 and 19 illustrate the burner used in the first campaign to test this idea. The burner uses a stoichiometric mixture of methane and air that flows from the bottom, and a spark ignitor is used to ignite the mixture inside the alumina foam. The ceramic wool is placed at the bottom and top of the iron bed as a filter, and a spring is

located at the top of the bed to keep it packed. This setup allows for the efficient preheating of the iron powders and initiation of the combustion reaction.

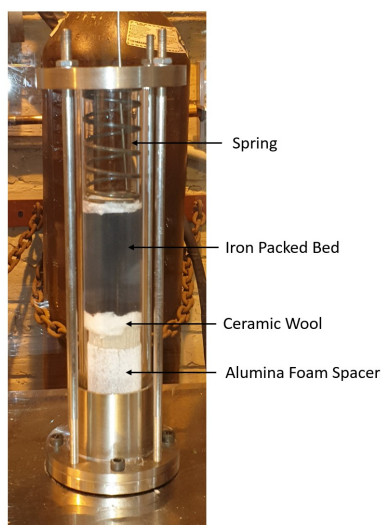


Figure 18: The reactor used in the first campaign

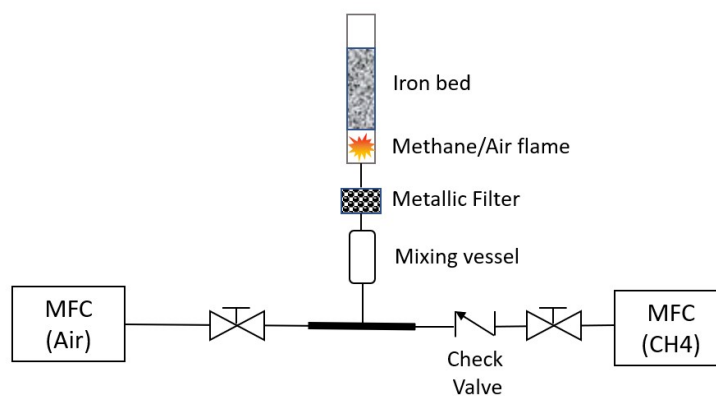


Figure 19: A simple sketch of the apparatus used in the first campaign

2.1.2 Electric Heater

In this iteration, Watlow ceramic fiber heaters [63] were used for preheating. These heaters are known for their high temperature heating elements and ability to reach temperatures up to 2200 °F, and a thick layer of ceramic fiber insulation is used to isolate the heating chamber.

During the second campaign, heating input air via these heaters was tested (Fig. 20 and 21). This was done by using three semi-cylindrical heaters to increase the air's temperature while it was passing through a stainless steel tube before flowing to the bed. This warm air preheated the bed until it reaches the desired temperature.



Figure 20: The apparatus used in the second campaign

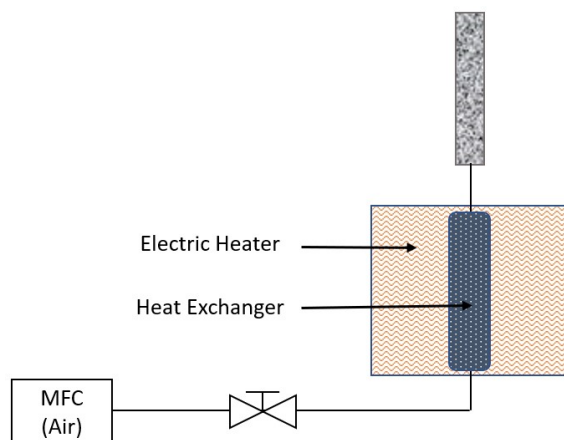


Figure 21: A simple sketch of the apparatus used in the second campaign

The results of these two campaigns, which is discussed in chapter 3, leads to our final design in which the heaters are placed around the combustion chamber to directly preheat the iron powders (Fig. 22 and 23).

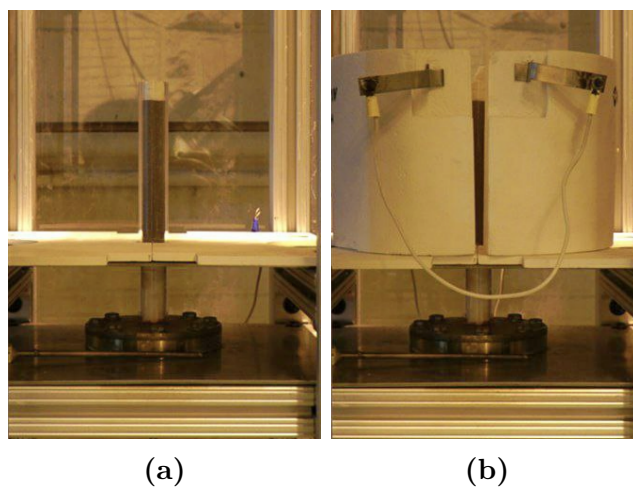


Figure 22: The apparatus used in the third campaign

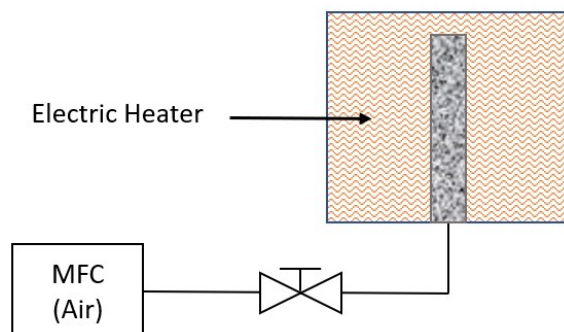


Figure 23: A simple sketch of the apparatus used in the third campaign

2.2 Sealing

Leakage was a significant issue in the first and second campaigns. To address this problem, a precise sealing calculation was performed for the final design, resulting in a more effective sealing system. The final burner design includes a quartz tube that is glued to a stainless steel disk, and the disk is screwed to a stainless steel flange that is connected to the gas line as illustrated in Figure 24. This design provides a more reliable seal, preventing gas leakage and ensuring the proper operation of the burner.

Silicon adhesive has been used to attach the quartz tube to the disk. The heaters and the iron bed are placed about 3 in above the joint (Fig. 22b) as not to degrade the quality of the sealant, given that the maximum operating temperature of the adhesive is 600°F. In the early tests of this campaign, ceramic adhesive, which is compatible with high temperature (3000 °F), was used; however, it was not successful due to the porous nature of ceramic, leading to leakage in the joint.

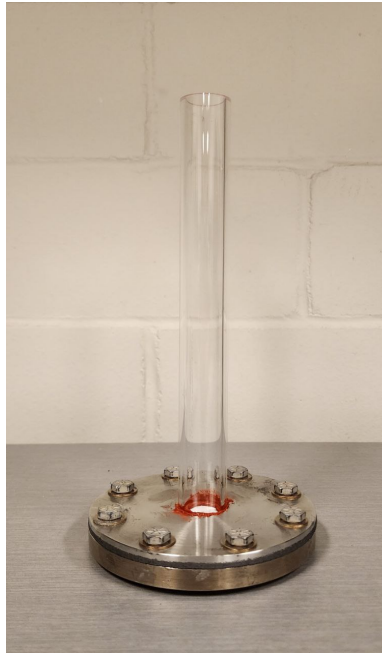


Figure 24: The apparatus used in the experiments

A graphite gasket is placed between the disk and the flange, and they are all bolted together. Fang et al. [64] suggested following seven steps to determine the required bolts torque for establishing a seal. These steps involve factors such as the size and material of the gasket, the number of bolts used, and the desired level of tightness for the seal. By following these steps, the final design of the burner is likely to be more effective at preventing gas leakage, leading to improved performance.

1. Minimum tightness parameter ($T_{P_{\min}}$):

$$T_{P_{\min}} = 0.1242 \times C \times P_D \quad (3)$$

Where C is a constant determined with respect to the tightness class, and P_D is the pressure inside the burner (psi).

2. Tightness ratio (T_r):

$$T_r = \frac{\log(1.5T_{P_{\min}})}{\log(T_{P_{\min}})} \quad (4)$$

3. Required theoretical seating stress (S_{ya} , psi):

$$S_{ya} = \frac{G_b}{e}(1.5T_{P_{\min}})^a \quad (5)$$

Where G_b and a are the intercept and slope of the tightness graph given by gasket manufacture. Moreover, e depends on the method of bolt seating, i.e., it is 0.75 for manual and 1 for machine.

4. Minimum design stress (S_m , psi): The highest value between seating stress component (S_{m2}), operating stress component (S_{m1}), and $2P_D$:

$$S_{m2} = \frac{S_{ya}}{1.5} - P_D \frac{A_H}{A_G} \quad (6)$$

$$S_{m1} = G_s \left(e \times \frac{S_{ya}}{G_s} \right)^{\frac{1}{T_r}} \quad (7)$$

Where A_H and A_G are the hydro static area and gasket area respectively:

$$\text{mean diameter of gasket: } G = \frac{OD + ID}{2} \text{ in} \quad (8)$$

$$A_H = \frac{\pi}{4}G^2 \quad , \quad A_G = \frac{\pi}{4}(OD^2 - ID^2) \text{ in}^2$$

5. Optimum bolt load (W_m , lb_f):

$$W_m = P_D A_H + S_m A_G \quad (9)$$

6. Actual bolt load (W_{mo} , lb_f)

$$W_{mo} = \frac{W_m}{0.85} \quad (10)$$

7. Required bolt torque (T, in.lbf/bolt):

$$\text{Force per bolt: } F_i = \frac{W_{mo}}{\text{number of bolts}} \quad (11)$$

$$T = F_i \times k \times D \quad (12)$$

Where D is the nominal bolt diameter, and k is the bolt friction factor. The bolt friction factor is generally lower for well-lubricated bolts, typically around 0.15, and for non-lubricated bolts, it is around 0.25. In this research, a mean value of 0.2 is

used as Fang et al. [64] suggested, which takes into account both lubricated and non-lubricated bolts.

Based on these steps and the given parameters of the APX2 graphite gasket [65] with $ID = 3$ in and $OD = 4.5$ in, a torque of approximately 180 in.lbf should be applied to eight 1/4 in-bolts to achieve a standard class of tightness ($C = 1$) in the final design of the burner when the air pressure inside the setup is assumed to be 2 atm (29.4 psi). The torque level is checked with a torque wrench to ensure the seal is tight enough.

2.3 Mass Flow Controller

Mass flow controllers (MFCs) are used to control the gas flow rate. In this research, SLA5800-series Brooks MFCs [66] are used, which are connected to a black box that allows them to communicate with a PC. The MFCs are calibrated using a DryCal ML-500 dry-piston [67], which is a primary standard flow calibrator. The use of calibrated mass flow controllers ensures that the results are accurate and can be replicated by others.

The uncertainty of MFC consists of linearity error and repeatability error which are 0.12% of full scale (5 SLPM = 83.3 cc/s) and 0.2% of the readings, respectively. Moreover, the DryCal provides an accuracy of 0.45% of the readings. The air is fed into the bed at 10 cc/s in the last campaign; therefore, the uncertainty of the airflow rate in this campaign is equal to 0.054 cc/s:

$$\text{Linearity Error of the MFC} = 0.12\%FS = 0.0012 \times 83.33 \text{ cc/s} = 0.010 \text{ cc/s}$$

$$\text{Repeatability Error of the MFC} = 0.2\%SP = 0.002 \times 10 \text{ cc/s} = 0.020 \text{ cc/s}$$

$$\text{Uncertainty of the MFC} = \omega_{\text{MFC}} = \text{Linearity Error} + \text{Repeatability Error} = 0.030 \text{ cc/s}$$

$$\text{Uncertainty of the DryCal} = \omega_{\text{DryCal}} = 0.45\%SP = 0.0045 \times 10 \text{ cc/s} = 0.045 \text{ cc/s}$$

$$\text{Uncertainty of the system} = \sqrt{\omega_{\text{MFC}}^2 + \omega_{\text{DryCal}}^2} = 0.054 \text{ cc/s} \quad (13)$$

2.4 Powders

Iron powders with spongy flake structure are used in this research (Fig. 25). They are produced from high purity iron ore by hydrogen reduction method, and the apparent density is between 1 and 1.5 g/cc. Table 2 represents the results of the screen analysis of these powders and shows the percentage of the powders that passed through different mesh sizes.

Mesh size	Min	Max
+20	–	2%
-20,+60	30%	70%
-60,+100	10%	35%
-325	–	12%

Table 2: Results of screen analysis of iron powders provided by the supplier [68]

In the last campaign, iron powders were mixed with nonporous spherical alumina ceramic powders to prevent melting. The mesh size of the ceramic particles is -48 (300 μm) [69].

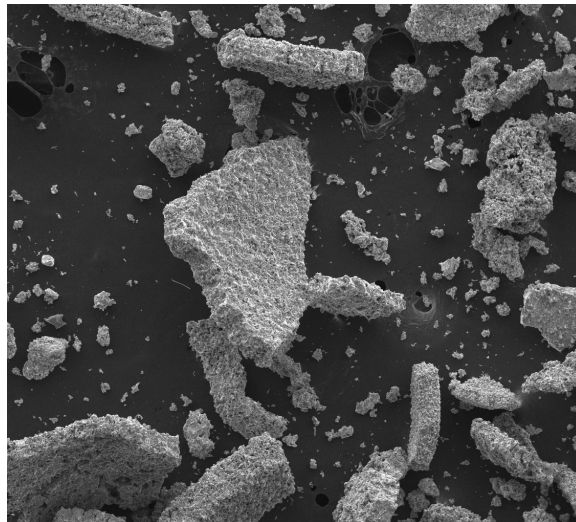


Figure 25: An SEM image taken from iron powders

2.5 Pressure Drop

A pressure drop occurs when a fluid passes through a porous medium due to frictional forces within the pores. It is important to accurately predict the pressure drop in this system in order to ensure that the downstream end of the bed has sufficient pressure to properly function.

Equation 14 is a widely used method for predicting the pressure drop in a packed bed of porous material proposed by Ergun in 1952 [70]. It describes the relationship between the pressure drop (ΔP), the length of the bed (L), the fluid viscosity (μ), porosity of the bed (ϵ), the fluid inlet velocity (u_0), the particle diameter (d_s), and the fluid density (ρ).

$$\frac{\Delta P}{L} = \frac{150\mu(1 - \epsilon^2)u_0}{\epsilon^3 d_s^2} + \frac{1.75(1 - \epsilon)\rho u_0^2}{\epsilon^3 d_s} \quad (14)$$

Equation 14 is specifically designed for porous beds consisting of spherical particles. If the particles in the bed have a different shape, a "sphericity factor" (ψ) should be used to modify Equation 14, resulting in Equation 16.

$$\psi = \frac{\text{surface area of sphere with equal volume to the nonspherical particle}}{\text{Surface area of the nonspherical particle}} \quad (15)$$

$$\frac{\Delta P}{L} = \frac{150\mu(1 - \epsilon^2)u_0}{\epsilon^3 d_s^2 \psi^2} + \frac{1.75(1 - \epsilon)\rho u_0^2}{\epsilon^3 d_s \psi} \quad (16)$$

In the final campaign, the airflow rate is constant at 3.5 cm/s passing through a 12-cm bed consists of highly porous iron particles and nonporous ceramic powders (Section 2.4). To estimate the pressure drop via the Ergun equation, it is assumed that the bed consists of 300-micron spherical powders. As the Figure 26 demonstrates, the pressure drop can be quite high in this case and can cause the quartz tube to become a pressure vessel, which is not desirable due to the brittle nature of quartz. To address this issue, a pressure relief valve is installed in the upstream of the bed with a set point of 25 psig.

In summary, this chapter discussed different aspects of an apparatus used to test the filtration combustion of a packed bed of iron powders. Various options were considered for preheating the iron powders, including using a methane/air flame or electric heaters. In the final campaign, the setup is perfectly sealed and involves a quartz tube attached to a stainless steel disk surrounded by the electric heaters. Air is fed to a bed consisting of spongy flake

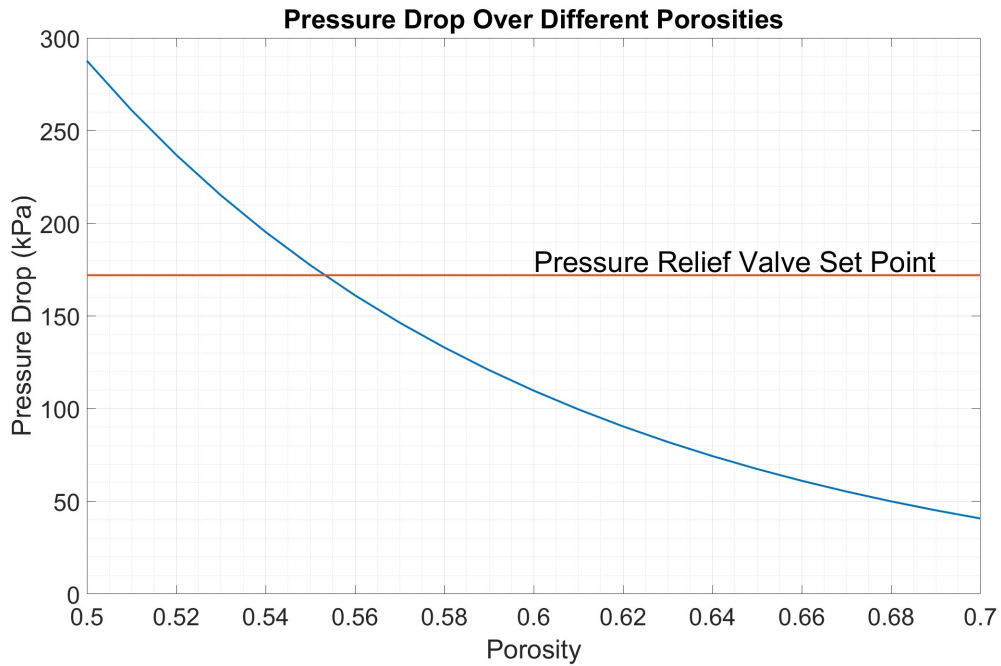


Figure 26: Pressure drop in a packed bed consists of spherical particles with $d = 300 \mu\text{m}$ while the airflow rate is 3.5 cm/s .

iron powders mixed with spherical ceramic particles. Moreover, a pressure drop occurs when air passes through the bed, and a pressure relief valve is installed to secure the apparatus.

3 Experiments

In this chapter, the methodology and results of the three campaigns are discussed.

3.1 First Campaign: Preheating Bed via Methane Air Flame

In the first campaign, a methane air flame is used for preheating the iron bed (Fig. 18).

3.1.1 Methodology

These experiments involves preheating the bed with the flame at a stoichiometric ratio ($\phi = 1$), then cutting off the methane and introducing air to the bed (Fig. 27). The range of airflow rates tested in this campaign is provided in Table 3.

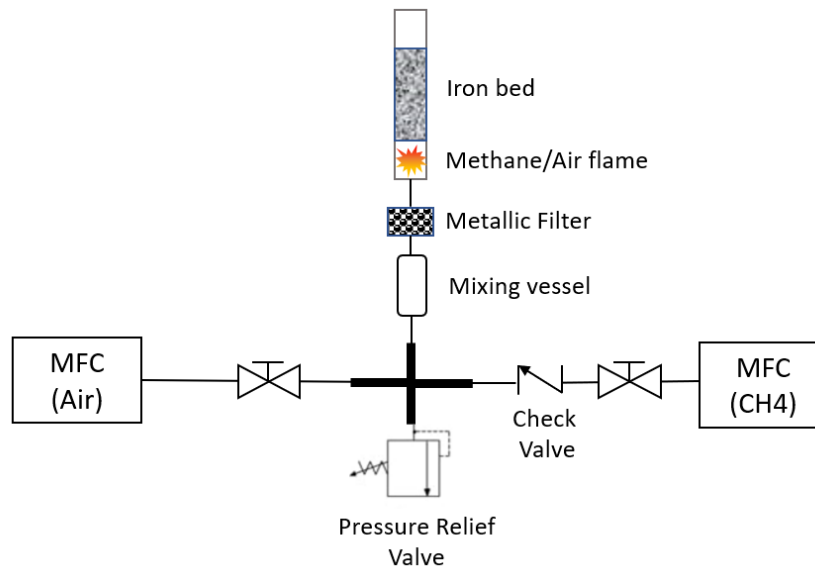


Figure 27: Diagram of the first campaign apparatus

Airflow Rate During Preheating ($\phi = 1$)	40 - 100 cc/s
Airflow Rate During the Iron Combustion	25 - 250 cc/s

Table 3: Range of the airflow rate tested in the first campaign

3.1.2 Results and Discussion

The qualitative behavior of this technology was examined in this campaign. Air is fed into the bed after the preheating, and an orange zone representing the combustion front is observed (Fig. 28). This orange zone slowly propagates from the bottom of the bed to the top as air is introduced.

Moreover, it is observed that increasing the airflow rate brightens the combustion zone, indicating a higher temperature at the combustion front and causing a considerable amount of melting inside the bed; on the other hand, decreasing the airflow rate quenches the reaction. Therefore, the reaction is controlled by the airflow rate. The same phenomena occurs in the smouldering combustion as increasing the airflow rate leads to transition to the flaming combustion.



Figure 28: The combustion front, first campaign

Furthermore, the results of this campaign points out two main problems that occur because of using a methane air flame for preheating at the bottom of the iron bed:

- The first problem is that a significant portion of the iron bed melts during this campaign, which is not desirable since it leads to the formation of channels inside the bed (Fig. 29), which can act as passages for air or hydrogen, causing an incomplete oxidation or reduction. Moreover, preventing sintering of powders is a laudable goal for any metal-based technologies since pulverising the metal consumes a considerable amount of energy.

This melting is particularly concentrated at the bottom parts of the bed that are exposed to the high-temperature methane air flame, i.e., the adiabatic flame temperature of methane, and air is around 2000°C , while the melting point of iron is 1538°C .



Figure 29: An oxidized iron bed produced in the first campaign

- The second problem is that the iron bed is partially oxidized with the hot water vapor (product of methane air combustion) during the preheating process which is visible in

the Figure 30 as colourful hydroxides formed on the surface of the bed. This oxidation before the combustion process reduces the efficiency of the system.



Figure 30: Colourful iron hydroxides ($\text{Fe}(\text{OH})_2$ and $\text{Fe}(\text{OH})_3$) produced during the preheating process.

3.2 Second Campaign: Preheating Air via Electric Heater

The second campaign is focused on addressing the problems encountered in the first campaign by using electric heaters for preheating instead of a methane air flame. This is done to avoid the issue of melting observed in the first campaign by controlling the preheating temperature.

3.2.1 Methodology

In the second campaign, three electric heaters are used for preheating the input air before it is introduced to the iron bed (Fig. 20).

Figure 31 demonstrates the setup of this campaign consisting of electric heaters, a pressure transducer, and thermocouples. The pressure transducer is used to track the pressure drop over the bed, while four k-type thermocouples, including T0, T1, T2, and T3, are used to

monitor the temperature of the inlet air, the bottom of the iron bed, the top of the iron bed, and the exhaust air, respectively. These sensors are connected to a data acquisition system called LabJack T7-Pro [71] which is used to record the data.

The air (Air 1) is passed through a heat exchanger that is filled with ceramic balls and placed inside the electric heaters. This hot air is then passed over the iron bed to raise its temperature. The initiation of combustion is determined by monitoring T1, i.e., when a sharp increase in T1 is observed, it means the combustion has initiated. The air supply is then switched to the cold air (Air 2), and the combustion front (orange zone) slowly propagates from the bottom to the top of the bed.

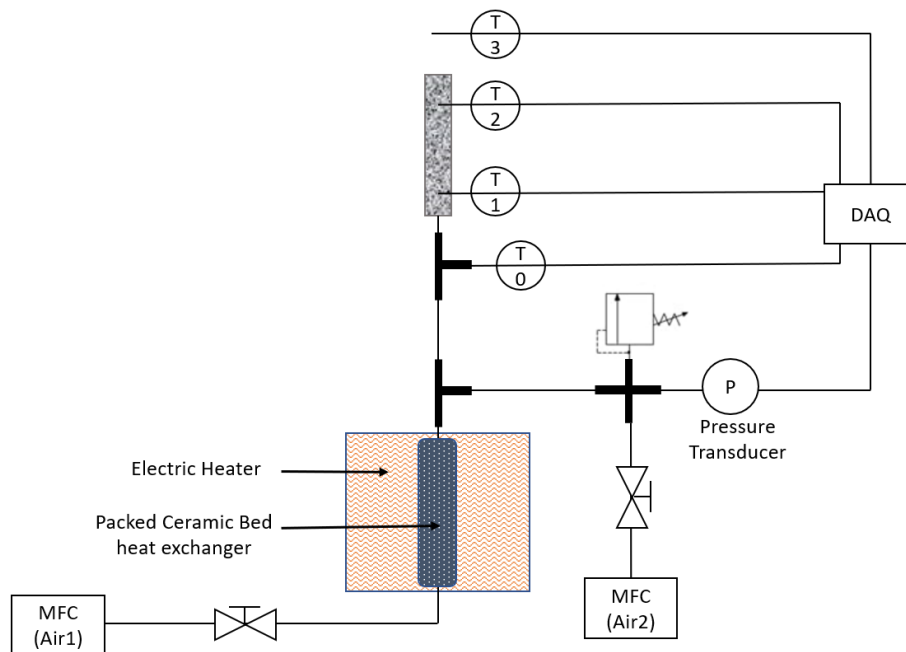


Figure 31: Diagram of the second campaign apparatus

3.2.2 Results and Discussion

This campaign provides a better understanding of the whole reaction by monitoring the temperature and the effect of heat loss on the system. The temperature of the inlet air (T_0) is measured over $800\text{ }^\circ\text{C}$ when the reaction initiates. Figure 32 demonstrates the temperature at the bottom (T_1) and top (T_2) of the bed from the moment the heater was turned on to when the orange zone (combustion front) was quenched in one of the experiments in this 28-test campaign. After about 45 minutes of preheating, a sharp inflection is observed in T_1 indicating the start of the reaction. The time delay between the peak of T_1 and T_2 implies the combustion front propagation.

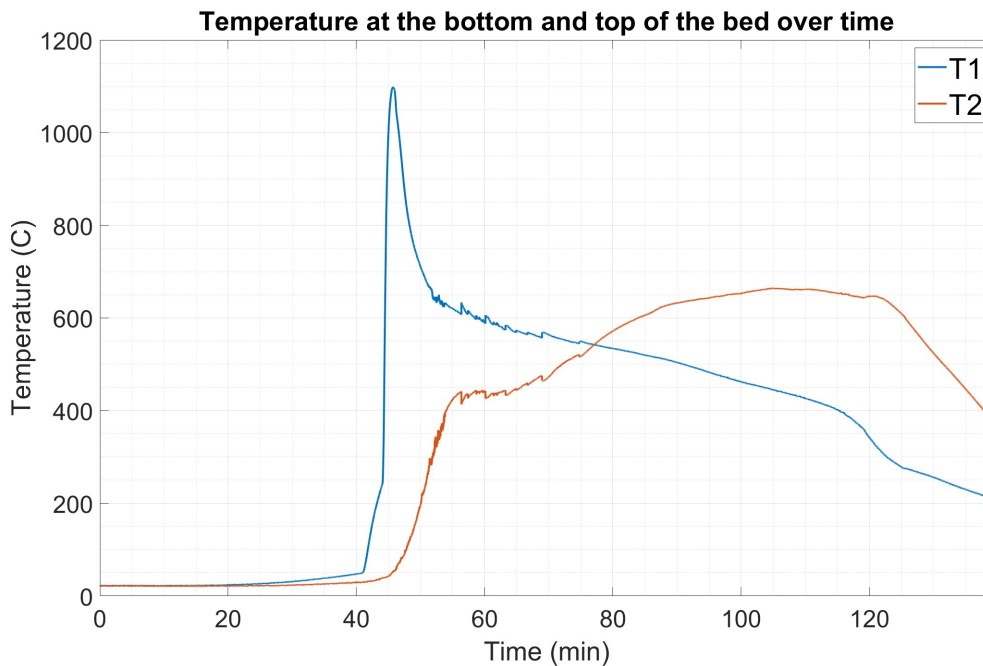


Figure 32: Temperature of the bottom (T_1) and top (T_2) of the iron bed in one of the tests in the second campaign

Temperature at the bottom of the bed (T_0) when the reaction initiates is much lower than the adiabatic flame temperature of methane/air which is about 2000 °C. Therefore, it is expected that using an electric heater for preheating the air prevents the melting of the iron bed which was one of the major issues of the first campaign; however, a small portion of the bed melts (Fig. 33) due to the high temperature resulting from heat generation during iron oxidation. To address this problem, in the third campaign, the iron powders are mixed with inert particles (ceramic powders) which absorb this heat and reduce the temperature of within the bed.



Figure 33: Melting within the bed in one of the tests of the second campaign

Additionally, the preheating time is considerably long (45 min) and during this time, the iron powders are exposed to the hot air blowing to the bed, leading to partial oxidation before the combustion. To avoid this problem and reduce the preheating time, in the third campaign, the heater is placed around the bed to preheat the iron powders directly instead of preheating the air.

The results of the second campaign also note that the system is highly sensitive to heat loss, i.e., covering the burner with thermal insulation (Fig. 34), using thermocouples with different

diameters, or thermocouples with various sheath materials can considerably affect the results. In conclusion, small changes can have impact on the heat loss which can significantly affect the overall performance and results of the system, and it is important to carefully control and monitor the heat loss in this system to obtain accurate and consistent results.



Figure 34: Placing ceramic wool as thermal insulation around the quartz tube to reduce the heat loss to the environment

3.3 Third Campaign: Preheating Bed via Electric Heaters

The last campaign aims to address the problems encountered in the first and second campaigns, by using ceramic powders mixed with iron powders to prevent melting, and also by placing the heater around the iron powders to reduce the preheating time and avoid partial oxidation before the combustion.

3.3.1 Methodology

Two semi-cylindrical radiant heaters are placed around a 1.9-cm-diameter quartz tube which is filled with a mixture of iron and ceramic powders. A thermocouple is used to monitor the heaters' temperature, and it is connected to a relay [72] and a PID controller [73] to maintain the temperature of the heaters around the set point (Fig. 35).

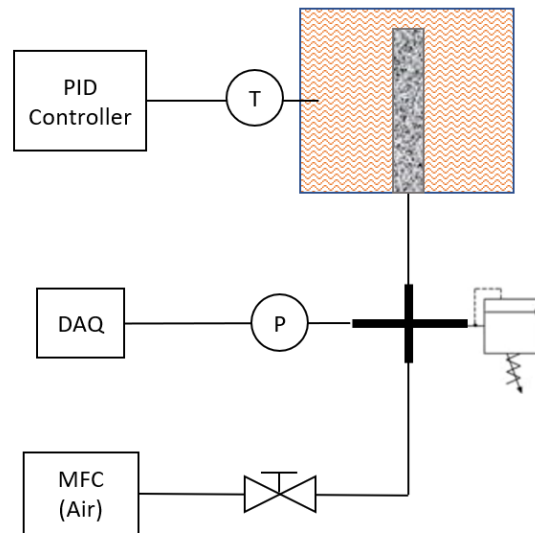


Figure 35: Diagram of the final apparatus

In these experiments, the heaters are heated up to 500 °C, then air is fed to the bed, and the combustion initiates. To control the heat loss, the heaters' temperature is kept constant at 500 °C during the test. Moreover, no thermocouple is placed inside the bed since the thermocouples work as heat sinks and affect the heat loss of the bed. Instead, the temperature is monitored via an infrared camera [74] through a narrow gap between the heaters (Fig. 22). The transmissivity of the quartz tube is considered in the IR Camera's

recordings; therefore, the measured temperatures of the bed surface are roughly accurate.

In summary, not using thermocouples inside the bed while the environment temperature is constant at 500 °C leads to have a better control of the heat loss and to have more accurate results.

3.3.2 Results and Discussion

In the second campaign, melting inside the bed is observed due to the considerable amount of heat generated as a result of combustion of iron powders, and to address this problem, the iron powders are mixed with inert particles (alumina ceramic powders) in this campaign.

Han [75] suggests Equation 17 to determine the temperature distribution in a cylindrical rod with internal heat generation where k is the conductivity of the rod, \dot{q} is the rate of heat generated inside the cylinder per volume (W/m^3), and c_1 and c_2 are constants, which are determined according to the boundary conditions.

$$T(r) = \frac{-\dot{q}r^2}{4k} + c_1 \ln r + c_2 \quad (17)$$

In a symmetric boundary condition (Fig. 36), temperature profile within the bed is:

$$T(r) = T_s + \frac{\dot{q}r_0^2}{4k} \left(1 - \frac{r^2}{r_0^2}\right) \quad (18)$$

Equation 18 can be used to estimate the maximum surface temperature (T_s) which does not

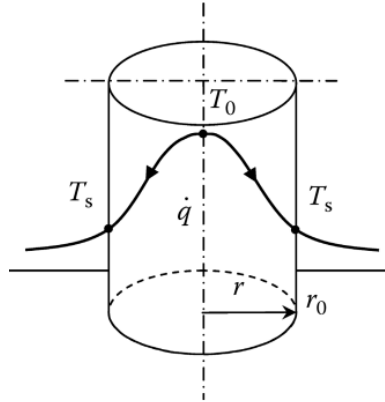


Figure 36: Cylindrical rod with internal heat generation [75]

lead to melting in the middle the bed, i.e., find T_s when the temperature at the center of the bed ($T(r = 0) = T_0$) is equal to 1800 K which is iron's melting point. This equation is based on the thermal conductivity of the bed (k) and the rate of generated heat per volume over the oxidation (\dot{q}).

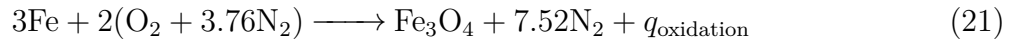
The effective conductivity of a porous material (k_e) depends on the conductivity of the solid (k_s), fluid (k_f), and porosity (ϵ). In this thesis, k_s is the conductivity of iron (80 W/m.k), k_f is the conductivity of air (0.026 W/m.k), and the porosity of the bed is estimated 0.81 by Equation 19.

$$\epsilon = \frac{\text{Volume of the Void Space}}{\text{Total Volume of the Bed}} = \frac{V_{\text{bed}} - \frac{m_{\text{iron powders}}}{\rho_{\text{iron}}}}{V_{\text{bed}}} \quad (19)$$

The geometric means model is used to determine the effective conductivity of the bed. According to this model [76], the effective conductivity can be calculated by taking the geometric mean of the conductivity of the solid and fluid (Equation 20).

$$k_e = k_f^\epsilon k_s^{1-\epsilon} \quad (20)$$

To determine the rate of heat generated by the reaction, the main product of the combustion is considered Fe_3O_4 :



$$q_{\text{oxidation}} = -(\sum N\bar{h}_{\text{products}} - \sum N\bar{h}_{\text{reactants}}) = \bar{h}_{f\text{Fe}_3\text{O}_4}^o \quad (22)$$

q_{gen} in Equation 23 takes into account the change in the enthalpy of the iron powders and the products due to the heating by the electric heaters.

$$q_{\text{gen}} = q_{\text{oxidation}} + (h_{T_{\text{heater}}}^o - h_{298.15}^o)_{\text{Fe}_3\text{O}_4} + 7.52(h_{T_{\text{heater}}}^o - h_{298.15}^o)_{\text{N}_2} - 3(h_{T_{\text{heater}}}^o - h_{298.15}^o)_{\text{Fe}} \quad (23)$$

The temperature of the heaters is constant at 500 °C, and the values of $h_{f\text{Fe}_3\text{O}_4}^o$ and Δh^o are taken from NIST Chemistry WebBook [77].

The heat generated per volume (W/m^3) can be calculated via Equation 24, where ρ_{air} is the density of air, u_{air} is the velocity of air fed into the bed, r_0 is the radius of the burner, and MW_{air} is the molar weight of air.

$$\dot{q}_{\text{gen}} = \frac{q_{\text{gen}} \rho_{\text{air}} u_{\text{air}} \pi r_0^2}{9.52 \text{MW}_{\text{air}}}$$

$$\dot{q} = \frac{\dot{q}_{\text{gen}}}{\text{length of the combustion zone} \times \pi r_0^2} \quad (24)$$

In this research, the combustion zone is defined the part of the bed which is over 1000 K. According to the experimental data resulted when air velocity is roughly 3.5 cm/s (10 cc/s air is fed into a 1.9-cm-diameter tube), the length of the combustion zone is about 4.3 cm when no ceramic powders used inside the bed (Fig. 37a) while it increases to 5.6 cm when just 10% of the volume of the bed consists of ceramic powders (Fig. 37b).

Figure 38 demonstrates the maximum surface temperature for burners with various diameters that does not cause melting in the center of the bed when air velocity is 3.5 cm/s, i.e., the temperature at the center of the bed is 1800 K (iron's melting point) and $u_{\text{air}} = 3.5 \text{ cm/s}$. The graph shows that for a burner with a diameter of 1.9 cm (the dimension of the quartz tube used in these experiments), the maximum surface temperature which does not lead to melting inside the bed is 1122 K for an iron bed and 1279 K for a bed contains 10% ceramic powders. This calculated temperature is higher than the surface temperature measured by the IR camera in an iron bed (Fig. 37a) and less than the surface temperature in a bed with 10% ceramic powders (Fig. 37b). Therefore, portions of the bed are expected to melt in the former case, while adding ceramic powders prevents melting in the latter case. Fig. 39 shows that the experimental results match with the prediction of this simple model, and adding

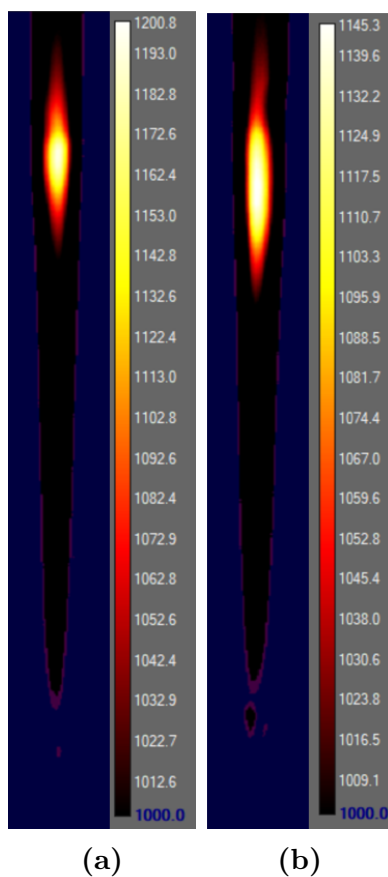


Figure 37: IR images showing the combustion zone in two different tests with various powder composition: a) No ceramic powders used. b) 10% of the volume of the bed consists of ceramic. Temperature bar is in Kelvin.

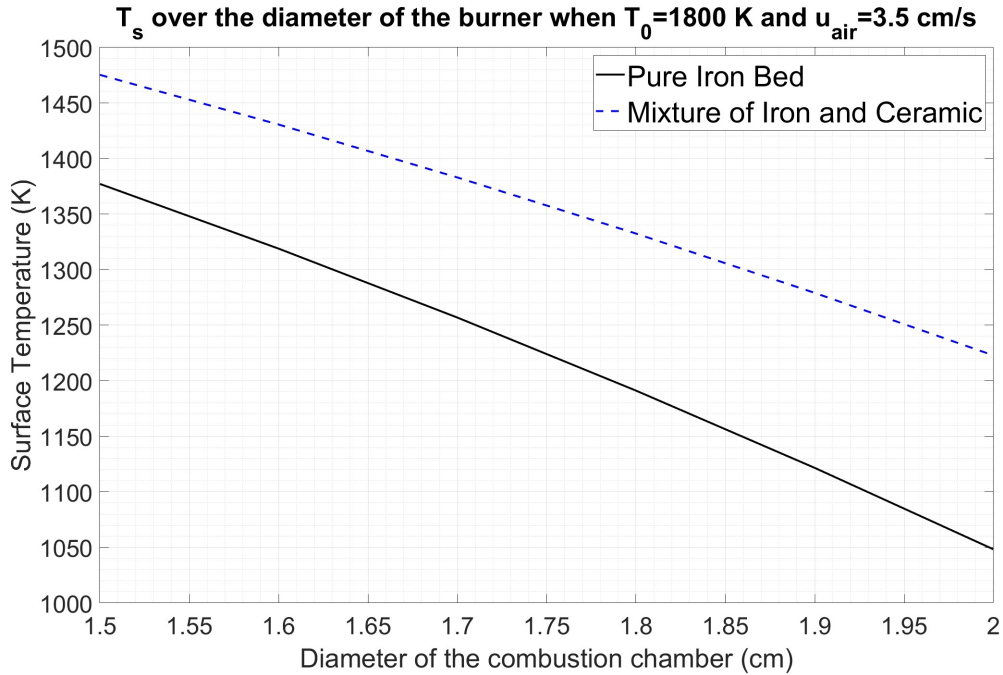


Figure 38: The maximum surface temperature which does not lead to melting inside the bed over the tube's diameter for a pure iron bed and when 10% of the volume of the bed consists of ceramic powders.

10% ceramic powders to the bed is sufficient enough to prevent melting when the airflow rate is 10 cc/s, and the tube's diameter is 1.9 cm.

Moreover, Fig. 38 indicates using smaller combustion chamber could lead to a more uniform temperature profile within the bed, avoiding melting at the center of the bed.

In conclusion, the rate of heat generation per volume (\dot{q}) determines the temperature of the bed, and mixing inert particles with iron powders decreases \dot{q} , lowering this temperature.

Similar to the observations of the previous campaigns, the combustion is controlled by airflow rate in these experiments. When the airflow rate is 5 cc/s, the combustion front is not observed inside the bed. However, when the airflow rate is increased to 10 cc/s, an orange

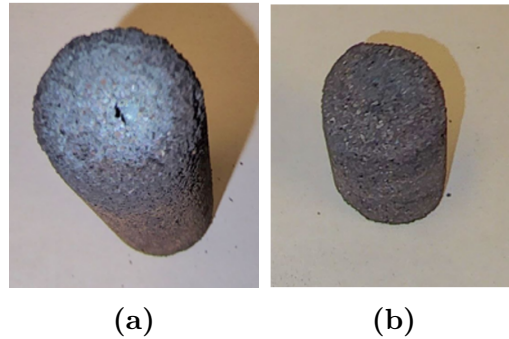
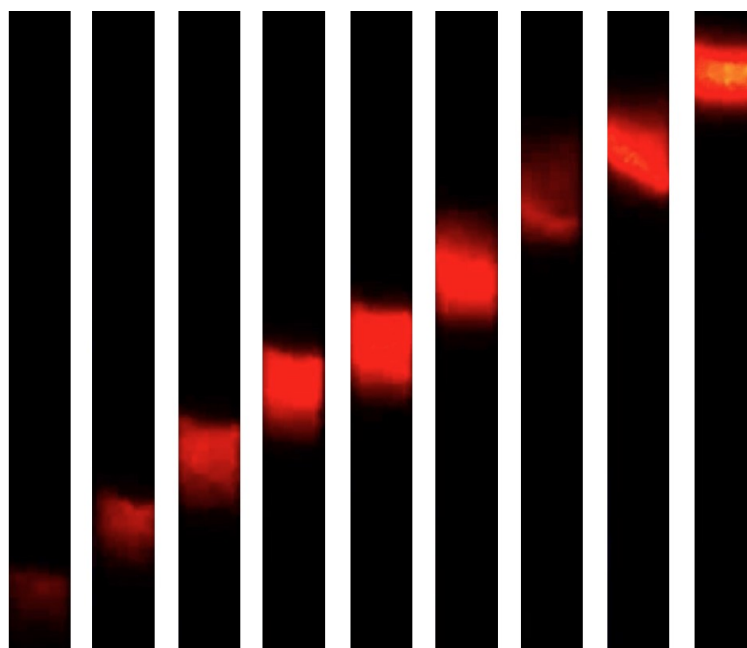


Figure 39: a) The gas channels resulted from melting inside the bed is observed in the oxidised bed when no ceramic powders mixed with iron powders. b) No melting is observed when 10% of the volume of the bed consists of ceramic powders, airflow rate = 10 cc/s and combustion chamber's diameter = 1.9 cm.

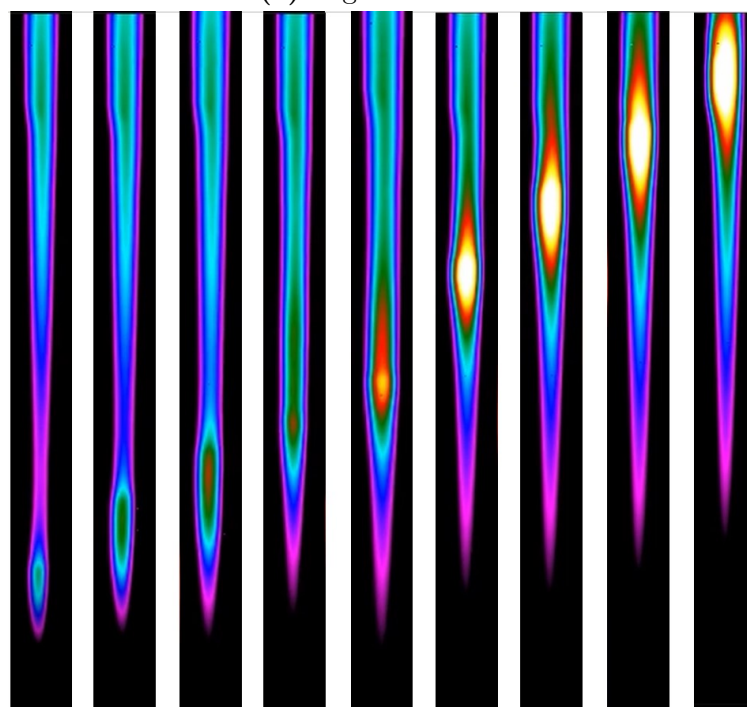
zone is generated, which slowly moves from the bottom of the bed to the top, as shown in Figure 40.

As the airflow rate is increased, the combustion front becomes hotter and propagates faster inside the bed. Figure 41 demonstrates the results of two different tests with the same powder content and various airflow rates (10 cc/s and 15 cc/s). It is observed that when the airflow rate is 10 cc/s and 15 cc/s, the combustion front passes along the bed in 55 min and 45 min, respectively. Moreover, the results of the experiments show that portions of the bed melt when the airflow rate is 15 cc/s and less than 40% of the volume of the bed consists of ceramic powders, while no melting is observed when over 10% of the volume of the bed consists of the ceramic powders and the airflow rate is 10 cc/s, meaning that the temperature of the bed with 10 cc/s airflow is lower than the temperature of the bed with 15 cc/s airflow.

In order to investigate the other effects of decreasing the rate of heat generation per volume

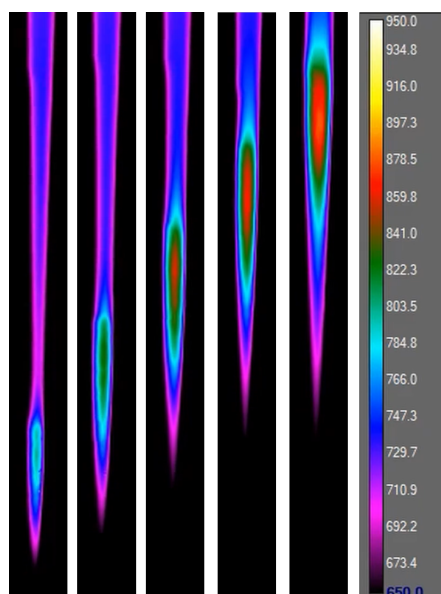


(a) Digital Camera

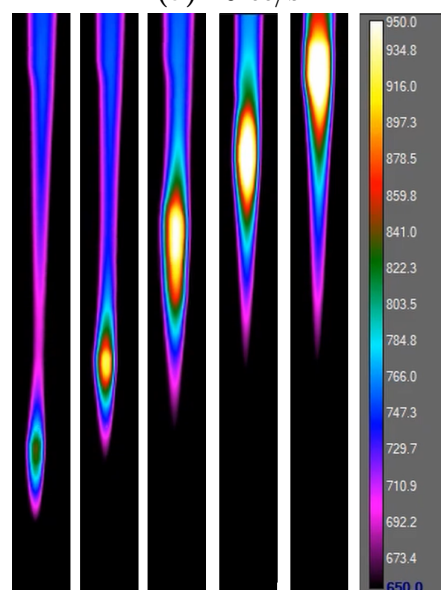


(b) IR Camera

Figure 40: Combustion front propagation during one test. The bed consists of iron powders (no ceramic is used) and airflow rate is 10 cc/s. Shots are taken in equal time steps.



(a) 10 cc/s



(b) 15 cc/s

Figure 41: Combustion front propagation during two different tests: 40% of the volume of the bed consists of ceramic powders, and airflow rate is a)10 cc/s and b)15 cc/s. Temperature bar is in Centigrade, and shots are taken in equal time steps.

by adding ceramic powders to the bed, the combustion of various powder compositions with a constant airflow rate of 10 cc/s is tested, i.e., a factor named CVR is defined (Equation 25) which is varying from 0% (pure iron bed) to 60% in the following experiments. The results of these tests are illustrated in Figure 42 and are also summarized in Table 4.

$$\text{Ceramic Volume Ratio (CVR)} = \frac{\text{Volume of the Ceramic Powders}}{\text{Total Volume of the bed}} \quad (25)$$

Table 4 provides information on the mass of iron powders (second row), mass of ceramic powders (third row), mass of the bed after the experiment (oxidized iron powders besides alumina particles, fourth row), as well as the amount of time it takes for the combustion front to propagate from the bottom of the bed to the top (fifth row).

Ceramic Volume Ratio (CVR)	0	10%	20%	30%	40%	50%	60%
Mass of Iron Powders (g)	51.6	50.0	48.1	41.9	36.1	30.2	23.3
Mass of Ceramic Powders (g)	0	8	15.4	23.6	31.1	40	47.2
Mass of the Oxidized Bed (g)	69	73	78	77	77	78	76
Time of the Test (min)	100	85	80	65	55	45	30

Table 4: Results of the tests with various powder compositions, campaign 3

The oxidized iron bed looks like a cartridge, and its solidity decreases as the CVR increases. Figure 43 demonstrates the appearance of the oxidized iron powder at different CVRs. As it is discussed, when $\text{CVR} = 0$ and $\text{airflow rate} = 10 \text{ cc/s}$, a small portion of the bed melts; however, adding ceramic to the bed prevents melting as it increases the length of the combustion zone (Figure 42).

Table 5 indicates the results of the XRD analysis performed on the oxidized powders.

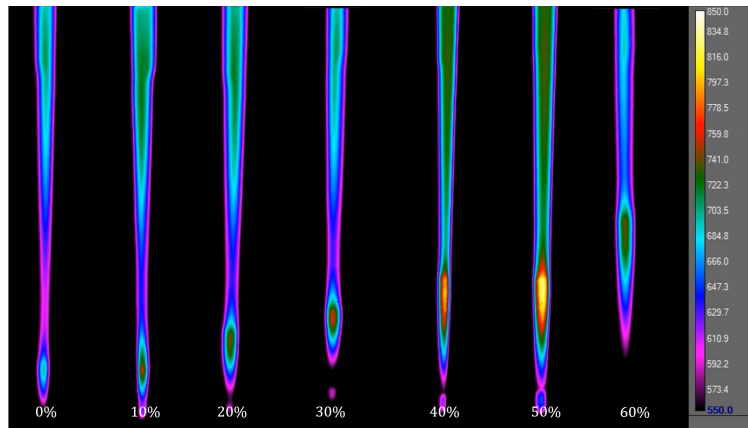
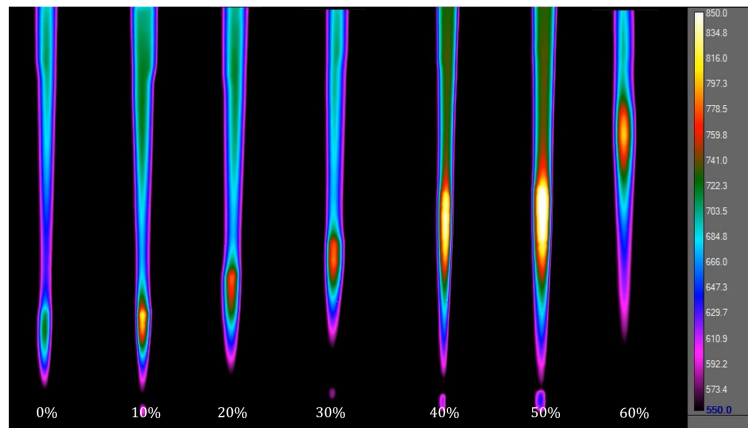
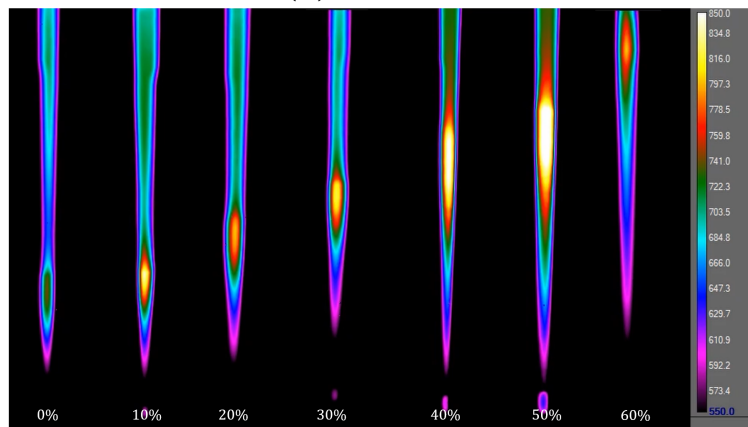
(a) $t = 10$ min(b) $t = 20$ min(c) $t = 30$ min

Figure 42: IR images of different tests over 30 minutes: airflow rate is 10 cc/s, and the CVR is different between 0% and 60%. Temperature bar is in Centigrade, and shots are taken in equal time steps

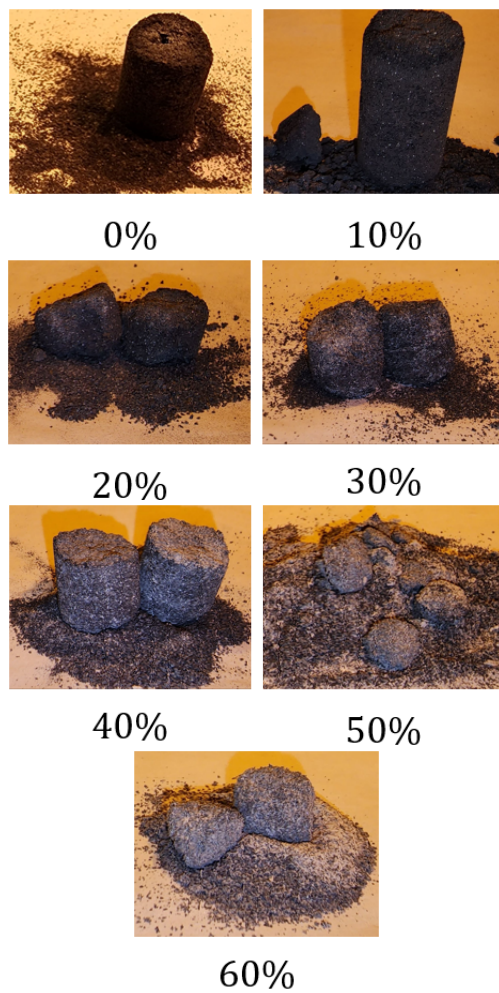


Figure 43: Oxidized bed produced in different tests with various powder compositions. Airflow rate is 10 cc/s, and the CVR is different between 0% and 60%

According to section 1.6, FeO is the main product of iron oxidation at high temperatures; however, it is not stable below 570°C and should be converted to Fe₃O₄ and Fe₂O₃ as the bed cools down. On the other hand, during the cooling process of the bed, the iron powders were not exposed to sufficient oxygen for this conversion to occur. Consequently, some amount of FeO was observed in the XRD analysis, although it's unstable at room temperature.

CVR	Fe(Wt.%)	Fe ₃ O ₄ (Wt.%)	Fe ₂ O ₃ (Wt.%)	FeO(Wt.%)	Al ₂ O ₃ (Wt.%)
0%	15.8	45.9	28.8	9.4	0
10%	10.2	36.8	34.9	9.7	8.4
20%	4.7	31.2	40.7	8.3	15.1
30%	10.2	35.6	26.0	5.0	23.2
40%	11.2	29.8	18.2	7.1	33.6
50%	4.9	17.8	17.0	4.9	55.4
60%	7.1	17.3	9.1	7.2	59.2

Table 5: Results of the XRD analysis conducted on the oxidized powders of various tests. Airflow rate is 10 cc/s, and the CVR is different between 0% and 60%.

The combustion efficiency is defined as the mass gained through the reaction over the mass that could be added in the case that all iron powders convert to Fe₃O₄, which is considered to be the ideal product in these tests (Equation 26).

$$\text{Combustion Efficiency} = \frac{m_{\text{oxidized bed}} - m_{\text{initial bed}}}{m_{\text{bed if all iron powders convert to Fe}_3\text{O}_4} - m_{\text{initial bed}}} \quad (26)$$

The combustion efficiency can be calculated according to the results of the XRD analysis, e.g., in no ceramic case (CVR = 0%), consider 100 g of oxidized powder, with the composition

determined by XRD, is available. The initial mass of iron in this sample can be calculated as follows

$$m_{\text{unburnt Fe}} = 15.8g \quad (27)$$

$$m_{\text{Fe in Fe}_3\text{O}_4} = 45.9g_{\text{Fe}_3\text{O}_4} \times \frac{1 \text{ mole}_{\text{Fe}_3\text{O}_4}}{\text{MW}_{\text{Fe}_3\text{O}_4}} \times \frac{3 \text{ mole}_{\text{Fe}}}{1 \text{ mole}_{\text{Fe}_3\text{O}_4}} \times \frac{\text{MW}_{\text{Fe}}}{1 \text{ mole}_{\text{Fe}}} = 33.21g \quad (28)$$

$$m_{\text{Fe in Fe}_2\text{O}_3} = 28.8g_{\text{Fe}_2\text{O}_3} \times \frac{1 \text{ mole}_{\text{Fe}_2\text{O}_3}}{\text{MW}_{\text{Fe}_2\text{O}_3}} \times \frac{2 \text{ mole}_{\text{Fe}}}{1 \text{ mole}_{\text{Fe}_2\text{O}_3}} \times \frac{\text{MW}_{\text{Fe}}}{1 \text{ mole}_{\text{Fe}}} = 20.14g \quad (29)$$

$$m_{\text{Fe in FeO}} = 9.4g_{\text{FeO}} \times \frac{1 \text{ mole}_{\text{FeO}}}{\text{MW}_{\text{FeO}}} \times \frac{1 \text{ mole}_{\text{Fe}}}{1 \text{ mole}_{\text{FeO}}} \times \frac{\text{MW}_{\text{Fe}}}{1 \text{ mole}_{\text{Fe}}} = 7.31g \quad (30)$$

$$m_{\text{Fe in initial bed}} = m_{\text{unburnt Fe}} + m_{\text{Fe in Fe}_3\text{O}_4} + m_{\text{Fe in Fe}_2\text{O}_3} + m_{\text{Fe in FeO}} = 76.46 \quad (31)$$

To determine the total mass of the initial bed, the mass of alumina mentioned in Table 5 should be added to the mass of iron.

$$m_{\text{initial bed}} = m_{\text{Fe in initial bed}} + m_{\text{Al}_2\text{O}_3} \quad (32)$$

Then, the mass of the bed if all iron powders converts to Fe_3O_4 can be determined according

to Equation 33.

$$m_{\text{Ideal}} = m_{\text{Fe in initial bed}} \times \frac{1 \text{ mole}_{\text{Fe}}}{\text{MW}_{\text{Fe}}} \times \frac{1 \text{ mole}_{\text{Fe}_3\text{O}_4}}{3 \text{ mole}_{\text{Fe}}} \times \frac{\text{MW}_{\text{Fe}_3\text{O}_4}}{1 \text{ mole}_{\text{Fe}_3\text{O}_4}} + m_{\text{Al}_2\text{O}_3} = 105.67g \quad (33)$$

In conclusion, 100 g oxidized powders with the composition determined by XRD are derived from 76.46 g initial powders. Moreover, assuming the entire iron powders in the initial bed ideally convert into Fe_3O_4 , the final mass after oxidation will be 105.67g. Therefore, the combustion efficiency determined via Equation 26 is

$$\text{Combustion Efficiency} = \frac{100 - 76.46}{105.67 - 76.46} = 0.81 \quad (34)$$

Table 6 demonstrated the calculated mass and combustion efficiency for each case.

CVR	Fe in Fe_3O_4	Fe in Fe_2O_3	Fe in FeO	m_{initial}	$m_{\text{final,ideal}}$	Combustion Eff.
0%	33.21	20.14	7.31	76.46	105.67	0.81
10%	26.63	24.41	7.54	77.18	103.45	0.87
20%	22.58	28.47	6.45	77.30	101.05	0.96
30%	25.76	18.19	3.89	81.23	103.40	0.85
40%	21.56	12.73	5.52	84.61	104.10	0.79
50%	12.88	11.89	3.81	88.88	101.67	0.87
60%	12.52	6.36	5.60	90.78	102.84	0.76

Table 6: Determining the mass of the initial bed for 100g oxidized powders according to the XRD results.

Furthermore, the combustion efficiency can be calculated by the mass of the bed at the beginning and end of the test , as reported in Table 4, and by determining the final ideal

mass using Equation 33.

Figure 44 demonstrates the values of the combustion efficiency for different cases, calculated through these two methods.

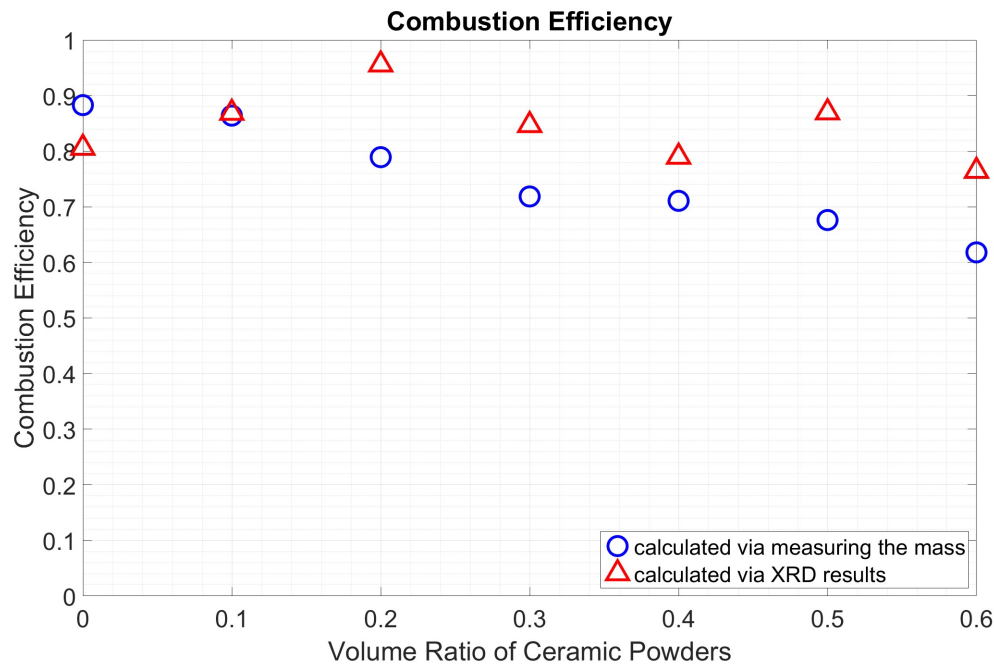


Figure 44: Combustion efficiency of different powder compositions, calculated according to the mass of the oxidized bed vs. results of the XRD analysis.

The oxidation of iron with air depends on temperature, as discussed in Section 1.6. Figure 40 demonstrates that the temperature of the reaction front is not constant during combustion. Therefore, the XRD analysis does not provide a comprehensive representation of the powder composition throughout the entire bed as it is conducted on a small portion of the bed. This leads to a difference between the combustion efficiency calculated by measuring the mass of the oxidized bed and the XRD analysis.

The combustion efficiency calculated by measuring the mass of the oxidized bed decreases as the CVR increases since raising CVR leads to a lower-temperature combustion inside the bed. However, the same result is not observed in the calculations using the XRD analysis due to the fact that the powders were not taken from the same location in each bed, resulting in oxidation occurring under different conditions.

Moreover, increasing CVR reduces the duration of the test as it decreases the amount of iron powders in the bed, i.e., Equation 35 indicates the relationship between the duration of the test and the mass of iron powders, and when the mass of iron powders decreases, the time of the test will also decrease.

$$\text{Time of the Test} = \frac{\text{mass of iron in the bed} \times W_{\text{air/iron}}}{\rho_{\text{air}} \times \dot{V}_{\text{air}}} \quad (35)$$

Where $W_{\text{air/iron}}$ is the mass of air required to oxidized one unite of mass of iron in Reaction 21, and \dot{V}_{air} is the flow rate of air (10 cc/s).

Equation 36 represents the relationship between the mass of iron powders and CVR.

$$\text{Mass of Iron in the Bed} = (1 - \text{CVR}) \times V_{\text{bed}} \times \rho_{\text{iron powders}} \quad (36)$$

If the values of Table 7 are plugged into Equation 35, the time of reaction can be calculated:

$$\text{Time of Reaction} = -117.6\text{CVR} + 117.6 \quad (37)$$

V_{bed}	$W_{\text{air/iron}}$	ρ_{air}	$\rho_{\text{iron powders}}$
35 ml	1.64	1.2 kg/m ³	1500 kg/m ³

Table 7: Properties of air and iron bed. Note that the density of a bed consisting of iron powders is considerably lower than the density of iron due to the porosity of the bed and powders.

Therefore, the duration of the test is predicted to be linearly dependent on the CVR as is observed in the experimental results shown in the Figure 45.

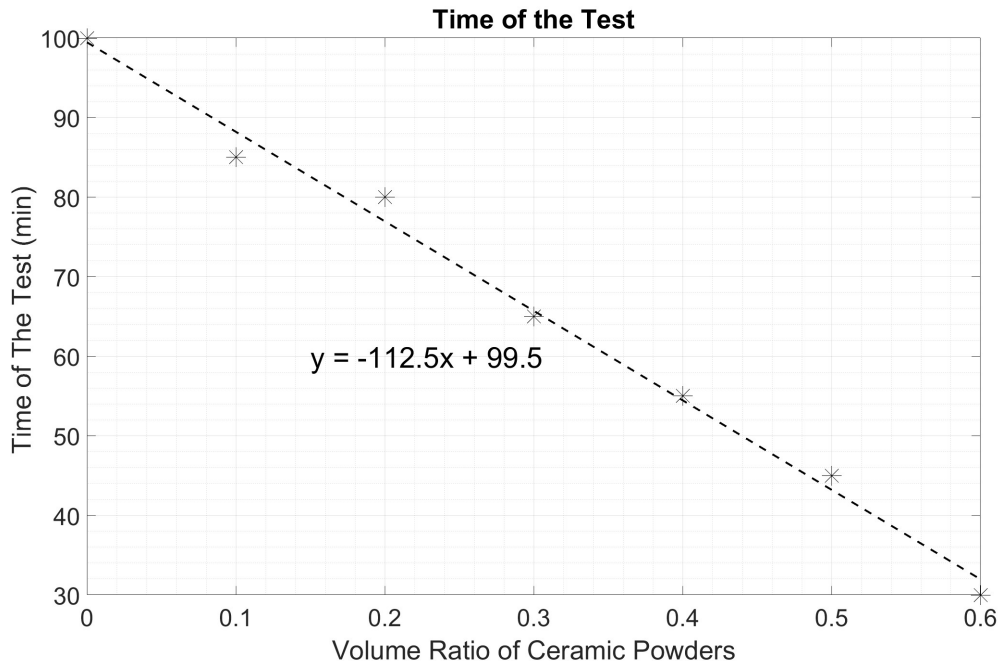


Figure 45: Time of the tests of various powder compositions.

The line generated from the experimental results slightly differs from the calculated line due to measurement errors, such as variations in the volume of the bed across tests (it is not precisely 35 ml in all the tests). Additionally, the combustion efficiency is less than 1 (Fig. 44), meaning that not all of the iron powders inside the bed are converted to Fe_3O_4 .

Knowing the time of the reaction and the length of the bed, the propagation speed can be estimated:

$$\text{Speed of the Combustion Wave} = \frac{\text{Length of the Bed}}{\text{Time of the Reaction}} \quad (38)$$

Figure 46 indicates the speed of the combustion wave in the tests, all of which had a bed length of 12 cm. The speed increases if CVR increases due to the decrease in the time of the reaction. Furthermore, the reported speeds are consistent with the range of speeds typically observed in a smouldering combustion which are 1 mm/min while the speeds in a flaming combustion are in order of 100 mm/min [78].

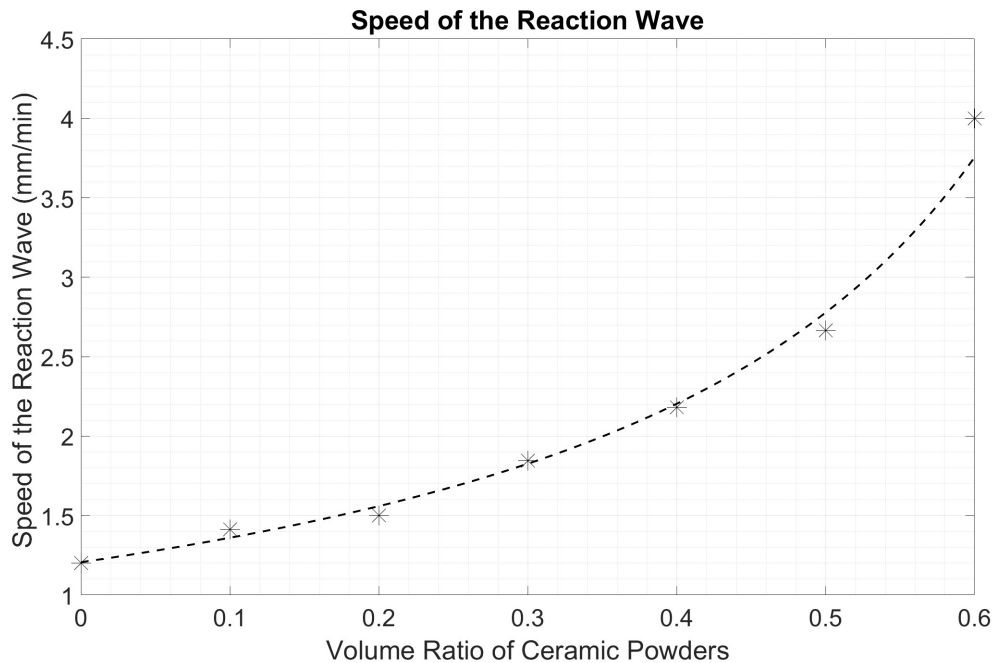


Figure 46: Propagation speed of the reaction wave of different powder composition

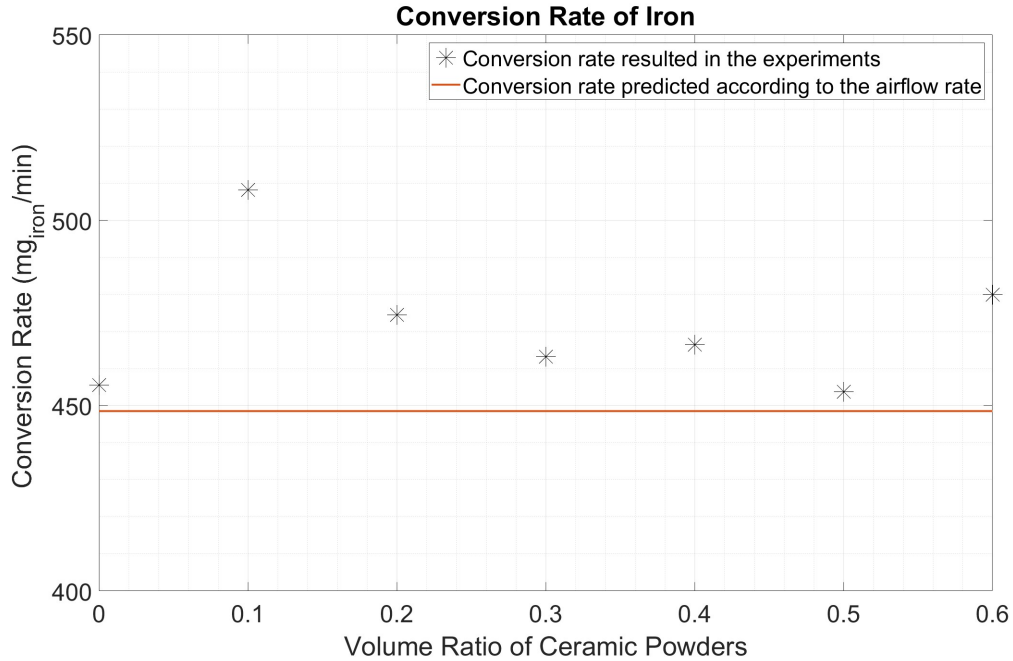


Figure 47: Conversion rate of iron to the iron oxides of different powder compositions

Another parameter that can be estimated is the rate at which iron powders convert to iron oxides (Equation 39). Figure 47 demonstrates this conversion rate.

$$\text{Rate of Iron Conversion} = \frac{\text{Mass of Iron Powders in the Bed} \times \text{Combustion Efficiency}}{\text{Time of the Reaction}} \quad (39)$$

The combustion efficiency calculated according to the mass of the bed is used to estimate the conversion rate. On the other hand, the conversion rate is expected to be constant since the airflow rate is constant in these experiments, i.e., the conversion rate can also be calculated according to the airflow rate (Equation 40). Considering the values of Table 7, the rate of

iron conversion is estimated to be 448.5 mg/min via this equation when $\dot{V}_{\text{air}} = 10$ cc/s.

$$\text{Rate of Iron Conversion} = \frac{\rho_{\text{air}} \dot{V}_{\text{air}}}{W_{\text{air/iron}}} \quad (40)$$

Furthermore, the rate of iron conversion can be estimated by the parabolic law discussed in Section 1.6. To find the conversion rate via Equation. 1, it is considered that the bed consists of solid spherical iron powders with a diameter = 300 μm and the temperature is 1000 K. At this temperature, 95% of the thickness of the oxide particle is FeO; thus, the other oxides layers (Fe_3O_4 and Fe_2O_3) could be neglected, and it is assumed that iron only converts to FeO:

$$\left| \frac{d_{m_{\text{Fe}}}}{d_t} \right| = \left| \frac{d_{m_{\text{FeO}}}}{d_t} \right| = \frac{\rho_{\text{FeO}} A_{\text{FeO}} k_{0,\text{FeO}} \exp\left(\frac{-T_{a,\text{FeO}}}{T}\right)}{X_{\text{FeO}}} \quad (41)$$

The formation of FeO occurs on the surface of the oxide layer:

$$A_{\text{FeO}} = 4\pi r_{\text{FeO}}^2 \quad (42)$$

$$r_{\text{FeO}} = r_{\text{Fe}} + X_{\text{FeO}}$$

Moreover, the Pilling-Bedworth ratio (PBR) of FeO oxidation is 1.7:

$$\text{PBR}_{\text{FeO}} = 1.7 \implies \frac{V_{\text{FeO}_{\text{final}}}}{V_{\text{Fe}_{\text{initial}}}} = \left(\frac{r_{\text{FeO}_{\text{final}}}}{r_{\text{Fe}_{\text{initial}}}} \right)^3 = 1.7 \implies \frac{r_{\text{FeO}_{\text{final}}}}{r_{\text{Fe}_{\text{initial}}}} = 1.19 \quad (43)$$

Where $V_{\text{Fe}_{\text{initial}}}$ and $r_{\text{Fe}_{\text{initial}}}$ are the volume and radii of the iron powders before the oxidation process initiates; moreover, $V_{\text{FeO}_{\text{final}}}$ and $r_{\text{FeO}_{\text{final}}}$ are the volume and radii of the FeO powder at the end of the oxidation process.

Over the oxidation, r_{Fe} changes from $r_{\text{Fe}_{\text{initial}}}$ to 0 while X_{FeO} differs from 0 to $1.19r_{\text{Fe}_{\text{initial}}}$. Therefore, assuming the values of Table 1, $T = 1000$ k, $r_{\text{Fe}_{\text{initial}}} = 150 \mu\text{m}$, $\rho_{\text{FeO}} = 5740 \text{ kg/m}^3$, the conversion rate of one iron particle ($\frac{dm_{\text{Fe}}}{dt}$) varies from 0.005 mg/min to 0.0003 mg/min during the test if the initial thickness of the oxide layer is considered $0.05r_{\text{Fe}_{\text{initial}}}$ instead of 0.

To find the conversion rate of iron inside the bed, the number of particles participating in the reaction should be estimated:

Rate of Iron Conversion = Number of Particles \times Conversion Rate of One Iron Particle

$$\text{Number of Particles} = \frac{\rho_{\text{Iron Bed}} \left(\frac{\pi}{4} d_{\text{tube}}^2 L_{\text{Combustion Zone}} \right)}{\rho_{\text{Iron}} \left(\frac{4\pi}{3} r_{\text{Fe}_{\text{initial}}}^3 \right)} \quad (44)$$

Where $\rho_{\text{Iron Bed}}$ is the density of the iron bed which is 1500 kg/m^3 , d_{tube} is the quartz tube diameter (1.9 cm), $L_{\text{Combustion Zone}}$ is the length of combustion zone considered 4.3 cm, and ρ_{Iron} is the density of iron (7900 kg/m^3). Indeed, Equation 44 estimates the number of spherical iron powders, which has a mass equal to the mass of the spongy flake iron powders reacting in the combustion zone. According to these assumptions, the iron conversion rate inside the bed changes from 850 mg/min to 50 mg/min during the test.

Note that temperature is estimated 1000 K in these calculations; however, over the experiments, it changes from room temperature to 1300 K. Moreover, more analysis should be done to gain a better understanding of the powders' morphology to improve the 300 μm -solid-spherical assumption in this model.

Another parameter which is measured during the tests is the pressure drop over the bed.

Figure 48 indicates this pressure drop over normalized time (time*):

$$\text{time}^* = \frac{\text{Time}}{\text{Time of the test mentioned in Table 4}} \quad (45)$$

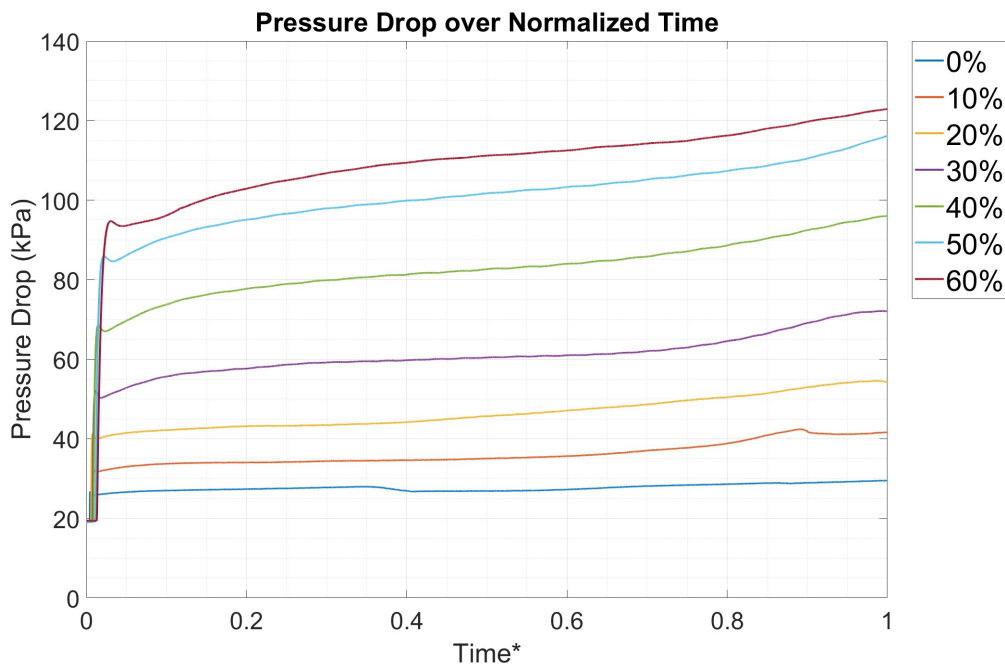


Figure 48: Pressure over the bed during test for various powder composition (CVR=0 to 60%)

Generally, pressure drop increases during a test since Pilling-Bedworth ratio of iron is higher

than one, i.e., the volume of the iron particles increases due to oxidation, decreasing the porosity of the bed.

Moreover, non-porous ceramic powders fill the empty spaces between the iron powders, which decreases the porosity; therefore, the pressure drop increases as CVR increases. Thus, the least amount of ceramic powders which does not lead to melting should be mixed with iron powders as increasing CVR causes an increase in the pressure drop over the bed, meaning a more powerful compressor should be used to provide the oxidizing airflow.

According to the experimental results, when CVR is 0, the pressure drop is 25.87 kPa at the beginning of the test, and the porosity of the bed is 0.81 (calculated by Equation 19); thus, $d_s\psi$ (Equation 16) is equal to 0.0000166. If the diameter of the powders (d_s) is assumed 300 micron, the sphericity factor (ψ) is about 0.80, meaning the iron powders are highly porous. Furthermore, this pressure drop increases to 29.61 kPa by the end of test. Assuming the $d_s\psi$ and V_{bed} are constant during the test, and oxidation only affect the porosity of the bed, ϵ is roughly 0.79 at the end of the oxidation process (ϵ_{final}). A decrease in the porosity is expected as PBR of Fe to Fe_3O_4 oxidation is 1.9.

Eventually, considering the ϵ_{final} is 0.79, the combustion efficiency calculated by Equation 46 is equal to 96.6%. This estimated value is roughly equal to the experimental findings (Fig. 44).

$$\epsilon_{\text{final}} = \frac{V_{\text{bed}} - (\text{PRB}_{\text{Fe}_3\text{O}_4} \times \eta_{\text{comb}} + (1 - \eta_{\text{comb}})) \frac{m_{\text{iron powders}}}{\rho_{\text{iron}}}}{V_{\text{bed}}} \quad (46)$$

Note that the combustion efficiency in other cases cannot be estimated via this method since Equation. 16 cannot be used to find the pressure drop over the bed consisting of iron and ceramic powders due to their different properties.

In conclusion, mixing ceramic powders with iron powders is a promising solution to prevent melting inside the bed. Moreover, the powder composition affects the combustion, i.e., increasing ceramic powders inside the bed decreases the reaction time and combustion efficiency, and it increases the speed of the combustion wave and pressure drop over the bed.

4 Conclusion

To assist the progress of creating a system for producing energy with zero pollutant emission via iron oxidation, a lab-scale burner was designed and built to study the filtration combustion of iron powders. This burner successfully indicated that a low-temperature combustion front slowly propagates through the iron bed.

Furthermore, in order to use this technology cyclically in oxidation and reduction processes, it is important to prevent melting inside the bed as it leads to the formation of passages for gases, resulting in incomplete oxidation or reduction over the bed. It was observed that mixing iron powders with inert ceramic particles can effectively address this problem and avoid melting within the bed. Therefore, this system has the potential to be successively charged and discharged as the iron powders keep unsintered due to adding ceramic powders to the bed.

Moreover, it was observed that the airflow rate plays a significant role in controlling this reaction, i.e., increasing the air flow rate can increase the temperature and speed of the combustion wave while decreasing the air flow rate can quench the combustion. Also, the composition of the powders affects the combustion inside the bed as increasing the amount of ceramic powders decreases the combustion temperature and combustion efficiency, and it increases the speed of the combustion wave and pressure drop over the bed.

In the future, this technology can work as an energy storage system for renewable energy sources, i.e., it can be used as a gas heater in a Brayton cycle to produce energy during

peak demand. Subsequently, the oxidized powders can be reduced by hydrogen over peak production.

This research focused on the oxidation of the iron bed. The reduction process and cyclability of the bed need to be investigated in future work. Possible next steps also include upscaling the burner and finding a more efficient way for preheating.

References

- [1] IPCC. *Climate Change 2021: The Physical Science Basis*. 2021. URL: <https://www.ipcc.ch/report/ar6/wg1/> (visited on 10/14/2022).
- [2] Marion King Hubbert. *Nuclear energy and the fossil fuels*. Vol. 95. Shell Development Company, Exploration and Production Research Division . . . , 1956.
- [3] NOAA. *Climate at a Glance*. 2022. URL: <https://www.ncei.noaa.gov/access/monitoring/climate-at-a-glance/global/time-series> (visited on 10/14/2022).
- [4] Tabbi Wilberforce, Ahmad Baroutaji, Bassel Soudan, Abdul Hai Al-Alami, and Abdul Ghani Olabi. “Outlook of carbon capture technology and challenges”. In: *Science of the total environment* 657 (2019), pp. 56–72.
- [5] Jon Gibbins and Hannah Chalmers. “Carbon capture and storage”. In: *Energy policy* 36.12 (2008), pp. 4317–4322.
- [6] Nadarajah Kannan and Divagar Vakeesan. “Solar energy for future world:-A review”. In: *Renewable and Sustainable Energy Reviews* 62 (2016), pp. 1092–1105.
- [7] Saidur Mekhilef, Rahman Saidur, and Azadeh Safari. “A review on solar energy use in industries”. In: *Renewable and sustainable energy reviews* 15.4 (2011), pp. 1777–1790.
- [8] John K Kaldellis and Dimitris Zafirakis. “The wind energy (r) evolution: A short review of a long history”. In: *Renewable energy* 36.7 (2011), pp. 1887–1901.

-
- [9] GM Joselin Herbert, Selvaraj Iniyan, E Sreevalsan, and S Rajapandian. “A review of wind energy technologies”. In: *Renewable and sustainable energy Reviews* 11.6 (2007), pp. 1117–1145.
- [10] Štefan Tkáč. “Hydro power plants, an overview of the current types and technology”. In: *Selected Scientific Papers-Journal of Civil Engineering* 13.s1 (2018), pp. 115–126.
- [11] Beatrice Wagner, Christoph Hauer, and Helmut Habersack. “Current hydropower developments in Europe”. In: *Current Opinion in Environmental Sustainability* 37 (2019), pp. 41–49.
- [12] Lorién Gracia, Pedro Casero, Cyril Bourasseau, and Alexandre Chabert. “Use of hydrogen in off-grid locations, a techno-economic assessment”. In: *Energies* 11.11 (2018), p. 3141.
- [13] Manish Kumar Singla, Parag Nijhawan, and Amandeep Singh Oberoi. “Hydrogen fuel and fuel cell technology for cleaner future: a review”. In: *Environmental Science and Pollution Research* 28.13 (2021), pp. 15607–15626.
- [14] Tianmei Chen, Yi Jin, Hanyu Lv, Antao Yang, Meiyi Liu, Bing Chen, Ying Xie, and Qiang Chen. “Applications of lithium-ion batteries in grid-scale energy storage systems”. In: *Transactions of Tianjin University* 26.3 (2020), pp. 208–217.
- [15] Boucar Diouf and Ramchandra Pode. “Potential of lithium-ion batteries in renewable energy”. In: *Renewable Energy* 76 (2015), pp. 375–380.

- [16] Hassan Nazir, Mariah Batool, Francisco J Bolivar Osorio, Marllory Isaza-Ruiz, Xinhai Xu, K Vignarooban, Patrick Phelan, Arunachala M Kannan, et al. “Recent developments in phase change materials for energy storage applications: A review”. In: *International Journal of Heat and Mass Transfer* 129 (2019), pp. 491–523.
- [17] Mahlia Mofijur, Teuku Meurah Indra Mahlia, Arridina Susan Silitonga, Hwai Chyuan Ong, Mahyar Silakhori, Muhammad Heikal Hasan, Nandy Putra, and SM Ashrafur Rahman. “Phase change materials (PCM) for solar energy usages and storage: An overview”. In: *Energies* 12.16 (2019), p. 3167.
- [18] Karolina Matuszek, Mega Kar, Jennifer M Pringle, and Douglas R MacFarlane. “Phase Change Materials for Renewable Energy Storage at Intermediate Temperatures”. In: *Chemical Reviews* (2022).
- [19] Jeffrey M Bergthorson. “Recyclable metal fuels for clean and compact zero-carbon power”. In: *Progress in Energy and Combustion Science* 68 (2018), pp. 169–196.
- [20] Philippe Julien and Jeffrey M Bergthorson. “Enabling the metal fuel economy: green recycling of metal fuels”. In: *Sustainable Energy & Fuels* 1.3 (2017), pp. 615–625.
- [21] Michael Soo, Xiaocheng Mi, Samuel Goroshin, Andrew J Higgins, and Jeffrey M Bergthorson. “Combustion of particles, agglomerates, and suspensions—A basic thermophysical analysis”. In: *Combustion and Flame* 192 (2018), pp. 384–400.

-
- [22] AL Breiter, VM Mal'tsev, and EI Popov. "Models of metal ignition". In: *Combustion, Explosion and Shock Waves* 13.4 (1977), pp. 475–485.
- [23] BI Khaikin, VN Blosenko, and A Go Merzhanov. "On the ignition of metal particles". In: *Combustion, Explosion and Shock Waves* 6.4 (1970), pp. 412–422.
- [24] AV Grosse and JB Conway. "Combustion of metals in oxygen". In: *Industrial & Engineering Chemistry* 50.4 (1958), pp. 663–672.
- [25] VI Bolobov. "Conditions for ignition of iron and carbon steel in oxygen". In: *Combustion, Explosion and Shock Waves* 37.3 (2001), pp. 292–296.
- [26] XiaoCheng Mi, Aki Fujinawa, and Jeffrey M Bergthorson. "A quantitative analysis of the ignition characteristics of fine iron particles". In: *Combustion and Flame* 240 (2022), p. 112011.
- [27] Irvin Glassman. *Metal combustion processes*. Tech. rep. Princeton Univ NJ James Forrestal Research Center, 1959.
- [28] Jeffrey M Bergthorson, S Goroshin, MJ Soo, P Julien, J Palecka, DL Frost, and DJ Jarvis. "Direct combustion of recyclable metal fuels for zero-carbon heat and power". In: *Applied Energy* 160 (2015), pp. 368–382.
- [29] Warren K Lewis and Edwin R Gilliland. *Production of pure carbon dioxide*. US Patent 2,665,972. Jan. 1954.

-
- [30] Juan Adánez, LUIS F de Diego, F Garcia-Labiano, P Gayán, A Abad, and JM Palacios. “Selection of oxygen carriers for chemical-looping combustion”. In: *Energy & Fuels* 18.2 (2004), pp. 371–377.
- [31] Mingchen Tang, Long Xu, and Maohong Fan. “Progress in oxygen carrier development of methane-based chemical-looping reforming: A review”. In: *Applied Energy* 151 (2015), pp. 143–156.
- [32] Xing Zhu, Yonggang Wei, Hua Wang, and Kongzhai Li. “Ce–Fe oxygen carriers for chemical-looping steam methane reforming”. In: *International journal of hydrogen energy* 38.11 (2013), pp. 4492–4501.
- [33] Zhen Huang, Fang He, Yipeng Feng, Rundong Liu, Kun Zhao, Anqing Zheng, Sheng Chang, Zengli Zhao, and Haibin Li. “Characteristics of biomass gasification using chemical looping with iron ore as an oxygen carrier”. In: *International journal of hydrogen energy* 38.34 (2013), pp. 14568–14575.
- [34] Nhut Minh Nguyen, Falah Alobaid, Paul Dieringer, and Bernd Epple. “Biomass-based chemical looping gasification: Overview and recent developments”. In: *Applied Sciences* 11.15 (2021), p. 7069.
- [35] Lu-lu Wang, Lai-hong Shen, Weidong Liu, and Shouxi Jiang. “Chemical looping hydrogen generation using synthesized hematite-based oxygen carrier comodified by potassium and copper”. In: *Energy & Fuels* 31.8 (2017), pp. 8423–8433.

- [36] Yu-Lin Kuo, Wei-Chen Huang, Wei-Mau Hsu, Yao-Hsuan Tseng, Young Ku, et al. “Use of spinel nickel aluminium ferrite as self-supported oxygen carrier for chemical looping hydrogen generation process”. In: *Aerosol and Air Quality Research* 15.7 (2015), pp. 2700–2708.
- [37] Zhongliang Yu, Yanyan Yang, Song Yang, Qian Zhang, Jiantao Zhao, Yitian Fang, Xiaogang Hao, and Guoqing Guan. “Iron-based oxygen carriers in chemical looping conversions: A review”. In: *Carbon Resources Conversion* 2.1 (2019), pp. 23–34.
- [38] Tao Song and Laihong Shen. “Review of reactor for chemical looping combustion of solid fuels”. In: *International Journal of Greenhouse Gas Control* 76 (2018), pp. 92–110.
- [39] Sander Noorman, Martin van Sint Annaland, and Kuipers. “Packed bed reactor technology for chemical-looping combustion”. In: *Industrial & engineering chemistry research* 46.12 (2007), pp. 4212–4220.
- [40] JC Abanades, Maria Elena Diego, and JR Fernández. “A novel air reactor concept for chemical looping combustion systems operated at high pressure”. In: *Chemical Engineering Journal* 390 (2020), p. 124507.
- [41] ME Diego and JC Abanades. “Experimental investigation of a diffusion-controlled chemical looping air reactor for energy storage applications”. In: *Chemical Engineering Journal* 428 (2022), p. 132083.

- [42] ME Diego and JC Abanades. “Techno-economic analysis of a low carbon back-up power system using chemical looping”. In: *Renewable and Sustainable Energy Reviews* 132 (2020), p. 110099.
- [43] AG Merzhanov and IP Borovinskaya. “Historical retrospective of SHS: An autoreview”. In: *International Journal of Self-Propagating High-Temperature Synthesis* 17.4 (2008), pp. 242–265.
- [44] AP Aldushin, AG Merzhanov, and BS Seplyarskii. “Theory of filtration combustion of metals”. In: *Combustion, Explosion and Shock Waves* 12.3 (1976), pp. 285–294.
- [45] Alvin Bayliss, Evgeny Shafirovich, and Vladimir A Volpert. “Counterflow combustion waves in short samples of metal powders at natural filtration of oxygen”. In: *Combustion Theory and Modelling* (2022), pp. 1–28.
- [46] Sergio Cordova, Kevin Estala-Rodriguez, and Evgeny Shafirovich. “Infiltration-controlled combustion of magnesium for power generation in space”. In: *Combustion and Flame* 238 (2022), p. 111950.
- [47] Alexander S Mukasyan, Sergey G Vadchenko, and Igor O Khomenko. “Combustion modes in the titanium-nitrogen system at low nitrogen pressures”. In: *Combustion and flame* 111.1-2 (1997), pp. 65–72.

-
- [48] SV Kostin, PM Krishenik, and KG Shkadinskii. “Experimental study of the heterogeneous filtration combustion mode”. In: *Combustion, Explosion, and Shock Waves* 50.1 (2014), pp. 42–50.
- [49] NS Evseev, M Kh Ziatdinov, VI Romandin, and AB Tolyzbekov. “Combustion of titanium and chromium powders in the co-flow of a nitrogen-argon mixture”. In: *Journal of Physics: Conference Series*. Vol. 1709. 1. IOP Publishing. 2020, p. 012011.
- [50] Janet L Ellzey, Erica L Belmont, and Colin H Smith. “Heat recirculating reactors: Fundamental research and applications”. In: *Progress in Energy and Combustion Science* 72 (2019), pp. 32–58.
- [51] M Abdul Mujeebu, M Zulkifyf Abdullah, MZ Abu Bakar, AA Mohamad, and MK Abdullah. “Applications of porous media combustion technology—a review”. In: *Applied energy* 86.9 (2009), pp. 1365–1375.
- [52] Thomas J Ohlemiller. “Modeling of smoldering combustion propagation”. In: *Progress in energy and combustion science* 11.4 (1985), pp. 277–310.
- [53] Guillermo Rein. “Smouldering combustion phenomena in science and technology”. In: (2009).
- [54] John Raymond Hall. *The smoking-material fire problem*. National Fire Protection Association Quincy, MA, 2010.

- [55] Muhammad A Santoso, Eirik G Christensen, Jiuling Yang, and Guillermo Rein. “Review of the transition from smouldering to flaming combustion in wildfires”. In: *Frontiers in Mechanical Engineering* 5 (2019), p. 49.
- [56] J Paidassi. “Sur l’oxydation du fer dans l’air dans l’intervalle 400°–700° C”. In: *Acta Metallurgica* 4.2 (1956), pp. 227–229.
- [57] MH Davies, MT Simnad, and CE Birchenall. “On the mechanism and kinetics of the scaling of iron”. In: *Jom* 3.10 (1951), pp. 889–896.
- [58] David John Young. *High temperature oxidation and corrosion of metals*. Vol. 1. Elsevier, 2008.
- [59] Carl Wagner. “Beitrag zur theorie des anlaufvorgangs”. In: *Zeitschrift für physikalische Chemie* 21.1 (1933), pp. 25–41.
- [60] Gregory J Yurek, John P Hirth, and Robert A Rapp. “The formation of two-phase layered scales on pure metals”. In: *Oxidation of Metals* 8.5 (1974), pp. 265–281.
- [61] G Garnaud and Robert A Rapp. “Thickness of the oxide layers formed during the oxidation of iron”. In: *Oxidation of Metals* 11.4 (1977), pp. 193–198.
- [62] WW Smeltzer and DJ Young. “Oxidation properties of transition metals”. In: *Progress in Solid State Chemistry* 10 (1975), pp. 17–54.

- [63] Watlow: Global Supplier of Industrial Electric Thermal Solutions. *Ceramic Fiber Heaters*. 2022. URL: <https://www.watlow.com/products/heaters/high-temperature-heaters/ceramic-fiber-heaters> (visited on 10/27/2022).
- [64] Jer-Pei Fang, Chi-Min Shu, Yu-Ching Chen, Shu-Ching Chen, and Mei-Ling Shyu. “Leakage evaluated and controlled from industrial process pipeline by optimum gasket assembly stress”. In: *Proceedings of the 17th Asia Pacific occupational safety & health organization conference, Taipei, Taiwan*. 2001, pp. 294–312.
- [65] TEADIT. *GR1700*. 2023. URL: <https://teadit.com/us/produto/gr-1700/> (visited on 01/17/2022).
- [66] BROOKS INSTRUMENT. *SLA5800 Series Mass Flow Controllers and Meters*. 2023. URL: <https://www.brooksinstrument.com/en/products/mass-flow-controllers/thermal-elastomer-sealed/sla5800-series> (visited on 01/11/2023).
- [67] MesaLabs. *ML-500 User and Manuals*. 2023. URL: https://www.tpf-control.nl/uploads/mesa-bios/ML-500-manual_RevJ.pdf (visited on 01/11/2023).
- [68] ChemicalStore.COM. *Iron Powder, Coarse, Mesh 20*. 2022. URL: <http://shop.chemicalstore.com/navigation/detail.asp?MySessionID=47-414847844&id=IRON12> (visited on 12/29/2022).

- [69] McMaster-Carr. *Non-Porous Alumina Ceramic Powder*. 2022. URL: <https://www.mcmaster.com/5092N117/> (visited on 12/29/2022).
- [70] Sabri Ergun. “Fluid flow through packed columns”. In: *Chem. Eng. Prog.* 48 (1952), pp. 89–94.
- [71] LabJack. *LabJack T7-Pro*. 2023. URL: <https://labjack.com/products/labjack-t7-pro> (visited on 01/10/2023).
- [72] OMEGA. *Solid State Relays with AC or DC Control Inputs*. 2023. URL: <https://www.omega.ca/en/control-monitoring/relays/solid-state-relays/ssrl240-660/p/SSRL240DC25> (visited on 01/11/2023).
- [73] OMEGA. *1/16, 1/8, AND 1/4 DIN Temperature and Process PID Controllers*. 2023. URL: <https://www.omega.ca/en/control-monitoring/controllers/pid-controllers/cnd3-series/p/CN16D3-S-AC> (visited on 01/11/2023).
- [74] Teledyne FLIR. *FLIR X6900sc MWIR*. 2023. URL: <https://www.flir.com/support/products/x6900sc-mwir/#Overview> (visited on 01/11/2023).
- [75] Je-Chin Han. *Analytical heat transfer*. Taylor & Francis, 2012.
- [76] OG Martynenko, NV Pavlyukevich, and OS Rabinovich. *Principles of Heat Transfer in Porous Media*, M. Kaviany, Springer-Verlag, New York (1991). 1993.

-
- [77] National Institute of Standards and U.S. Department of Commerce Technology. *NIST Chemistry WebBook*. 2022. URL: <https://webbook.nist.gov/chemistry/> (visited on 12/21/2022).
- [78] Hons K Wyn, Muxina Konarova, Jorge Beltramini, Greg Perkins, and Luis Yermán. “Self-sustaining smouldering combustion of waste: A review on applications, key parameters and potential resource recovery”. In: *Fuel processing technology* 205 (2020), p. 106425.